Chemical Engineering & Processing: Process Intensification 216 (2025) 110366

Contents lists available at ScienceDirect

Chemical Engineering and Processing - Process Intensification

journal homepage: www.elsevier.com/locate/cep

Less pressure loss with extra packing — The counterintuitive behavior of rotating packed beds

Felix Febrian [a,*], Georg Brösigke [a], Paul H. Kamm [b], Jens-Uwe Repke [a]

[a] Technische Universität Berlin, Process Dynamics and Operations Group, Sekr. KWT 9, Straße des 17. Juni 135, 10623 Berlin, Germany
[b] Helmholtz-Zentrum Berlin für Materialien und Energie, Hahn-Meitner-Platz 1, 14109 Berlin, Germany

ARTICLE INFO

Keywords:
HiGee
Rotating packed bed
Computational fluid dynamics
Virtual reconstruction
Open-cell foams

ABSTRACT

The Rotating Packed Bed (RPB), as a process intensification unit in heat and mass transfer of multiphase processes, has been gaining growing attention in recent years as reflected in the numerous investigations of the device. However, many questions remain unanswered regarding the fluid dynamics in RPBs, including the counterintuitive behavior of higher dry pressure drop in operations with empty rotor compared to operations with packed rotor. To address this issue, we employ numerical methods to acquire a detailed description of the fluid flow inside the device. The metal foam as the packing material is resolved through reconstruction techniques found in the literature. The simulation results reveal that the absence of packing, due to conservation of angular momentum, induces higher local velocities and therefore higher pressure loss. Further, we derive fundamental mechanism of the pressure loss inside the RPB from the local data that can potentially enhance existing correlations.

1. Introduction

The Rotating Packed Bed (RPB) and other related high-gravity devices have gained growing attention in recent years. These devices are often considered as a prime example for process intensification with use cases in absorption, stripping, distillation, gas–liquid reaction, nanoparticles preparation, polymerization, liquid degassing, and many others [1–6]. The terminology "high-gravity" refers to the application of centrifugal forces that exceed the gravitational force by several orders of magnitude. In the case of the RPB, the centrifugal acceleration is accomplished by rotating an annular rigid bed. The rotating part of the RPB, often denoted as the rotor, commonly contains a stainless steel wire mesh or metal foam as packing material. As portrayed in Fig. 1, liquid, or the fluid with higher density, is distributed onto the packing at its hollow center, where it flows outwards due to the centrifugal force. The other phase with lower density most often flows from the casing radially inwards through the packing in a counter-current manner driven by pressure difference. Aside of the counter-current process, co-current and cross-current flows are also possible in RPBs.

The high-gravity field is believed to lead to intensification of mass transfer of the two phases due to two reasons [7]. On one hand, the high centrifugal forces produce high velocities of the liquid, which in turn lead to a thinner boundary layer in the liquid phase and ultimately increased liquid side mass transfer coefficient. On the other hand, high interfacial area between the two phases is also realized. This intensification incentivized authors in the past to study the application of RPBs for absorption [8–10] or distillation processes [11,12]. Advantages achievable through this mass transfer intensification include a more compact design of the RPB, especially compared to conventional columns for thermal separation. Further potentials of the RPB are possible through its rotational speed, which poses an additional degree of freedom for a more flexible operation and less sensitivity of the equipment to outside movement, enabling installations of the equipment on floating vessels such as oil platforms.

Regarding the fluid dynamics of the RPB, numerous studies have attempted to derive correlations for important process parameters. Liu et al. [13] and Zheng et al. [14] presented pressure drop semi-empirical correlations based on simplified Navier–Stokes equations with parameters that need to be regressed for each individual RPB. Neumann et al. [15] developed a semi-empirical correlation for the dry pressure drop in RPB through a systematic evaluation of experimental data. Their correlation has been applied in further investigations, for instance in the extension of pressure drop as part of mass transfer modeling in distillation [11] or in the pressure drop study of a two-rotor RPB [16]. However, similar to our experiments, Neumann et al. [15] also observed that RPB operations with packing inside the rotor

* Corresponding author.
E-mail addresses: f.febrian@tu-berlin.de (F. Febrian), georg.broesigke@tu-berlin.de (G. Brösigke), paul.kamm@helmholtz-berlin.de (P.H. Kamm), j.repke@tu-berlin.de (J.-U. Repke).

https://doi.org/10.1016/j.cep.2025.110366
Received 11 March 2025; Received in revised form 5 May 2025; Accepted 16 May 2025
Available online 3 June 2025

Nomenclature

Latin Symbols

a	Specific area, $m^2\,m^{-3}$
A	Area, m^2
$A_{channel}$	Cross-sectional area of the foam sample, m^2
d_{char}	Characteristic diameter, m
d_C	Cell/sphere diameter, m
d_N	Node diameter, m
d_p	Pore diameter, m
h	Height, m
I	Turbulence intensity, –
k	Turbulent kinetic energy, $m^2\,s^{-2}$
L	Angular momentum, $kg\,m^2\,s^{-1}$
l	Length, m
m	Mass, kg
n	Rotational speed, RPM
Δp	Pressure drop, Pa or mbar
p	Static pressure, Pa or mbar
p_{total}	Total pressure, Pa or mbar
r	Radius, m
r_i	Inner radius of the rotor, m
r_o	Outer radius of the rotor, m
$r_{p,o}$	Outer radius of the metal foam packing, m
U_φ	Tangential velocity, $m\,s^{-1}$
U_r	Radial velocity, $m\,s^{-1}$
U_s	Superficial velocity, $m\,s^{-1}$
$\overline{U}$	Mean velocity, $m\,s^{-1}$
U'	Turbulent velocity fluctuation, $m\,s^{-1}$
w	Width, m
F	Volumetric flow rate, $m^3\,h^{-1}$

Greek Symbols

δ	Average cell length, m
ε	Porosity, –
ρ	Density, $kg\,m^{-3}$
ν	Kinematic viscosity, $m^2\,s^{-1}$
ω	Specific turbulence dissipation, s^{-1}
ω_r	Angular velocity, s^{-1}
ϑ	Temperature, °C

Dimensionless Numbers

Ma	Mach number
Re	Reynolds number

Abbreviations

CFD	Computational Fluid Dynamics
MRF	Multiple Reference Frame
NS	Navier–Stokes
RANS	Reynolds-averaged Navier–Stokes
RPB	Rotating Packed Bed
RPM	Rotations per minute
RZB	Rotating Zigzag Bed
STL	Stereolithography
VOF	Volume of Fluid

exhibit a lower pressure difference between gas inlet and gas outlet compared to operations without packing in the rotor. These results are remarkable and contraintuitive as the presence of packing material typically induces additional pressure loss due to friction in conventional packed bed columns. Furthermore, the correlation by Neumann et al. [15] underpredicted the conducted experiments without packing in the rotor. These findings indicate that the existing correlations are not able to completely explain the underlying mechanism of pressure loss inside RPBs yet. The comprehension of the mechanism is relevant for the generalizability of the correlation.

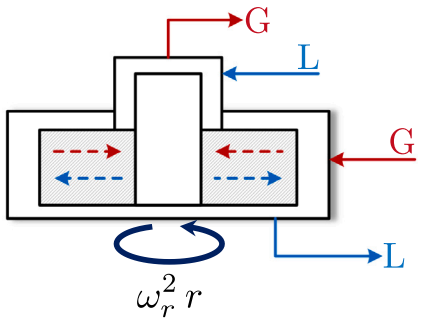

Fig. 1. Schematic drawing of the working principle of a RPB in counter-current mode.

Beside the pressure drop, another important aspect of the fluid dynamics for any thermal separation equipment is the phase distribution. Qualitative visual studies by Burns and Ramshaw [17] and Guo et al. [18] suggested that liquid flows in RPB's packing in form of rivulets and droplets instead of film flow on the packing's surfaces. Through the method of electric conductance measurements, Bašić and Duduković [19] and Burns et al. [20] developed an empirical correlation for the liquid holdup in relation to various operating parameters such as the liquid flowrate and rotational speed. More sophisticated measurements for liquid holdup include X-ray [21] and gamma ray [22,23] computed tomography. Nonetheless, currently applied experimental methods cannot measure the exact flow morphologies and local effective surface of the gas–liquid flow inside the packing, which is one of the key quantities in determining heat and mass transfer rates during thermal separation processes. These missing informations inhibit the development of reliable process models for RPB which could be vital for a widespread acceptance of the device in the chemical industry.

To address the lack of knowledge regarding the fluiddynamic previously described, local measurements inside the RPB are necessary. As they are not always feasible due to the rotating parts of the equipment, we moved to Computational Fluid Dynamics (CFD) as a tool to gain more insights into the physics. Llerena-Chavez and Larachi [24] first utilized porous media model for a single phase simulation in a RPB. The utilization of porous media model has since been adapted by other authors [25–27]. Many of the single phase simulations were performed to predict the overall pressure drop or to perform geometry optimization of the RPB. Aside of single-phase simulations, multiphase simulation frameworks such as the Volume of Fluid (VOF) method [28,29] or the Eularian model [30] have also been applied in simulations of RPBs. The applied multiphase models have been able to describe the liquid form, liquid velocity, and the holdup. It has also been reported that the multiphase model can be combined with a passive scalar to describe the mass transfer in the RPB. Further comprehensive review of CFD modeling for RPBs can be taken from [31].

Many of the multiphase simulations in RPB simplified the packing as quadrilateral or round rods spread across the rotor in a two dimensional domain. However useful, the assumption of two dimensional rods reduces the ability of the simulation to capture more complex liquid flow as shown in the more resolved three dimensional wire mesh conducted by Zhang et al. [32]. For this reason, we resolve the metal foam packing utilized in our experiments for our simulations. We employ a reconstruction workflow for the foam structure found in the literature [33,34].

The goal of this study is to explain the underlying cause for differences in pressure loss between operations with and without packing. In the process, we verify the feasibility of the metal foam reconstruction workflow for its application in RPB simulations. In this study, we will focus on the application of the reconstructed foam for single-phase flow. Naturally, the reconstruction workflow for the foam structure must be first validated. The rest of this work is therefore structured as follows. In the next section, we describe both the experimental setup

for metal foam validation and the RPB pressure drop measurements. Section 3 contains a brief description of the reconstruction workflow and the simulation cases that corresponds each experimental setup. Subsequently, pressure drops from the CFD simulations are compared and validated with the experiments in Section 4. Further, the local quantities obtained from the numerical simulations are analyzed to gain insights into the underlying physics.

2. Experimental setup

The experiments conducted in this study pursue two main objectives. Firstly, to validate and to parametrize the foam reconstruction workflow, an isolated sample of the nickel-chromium foam of product type NCX1116 from RECEMAT International later applied as packing inside the RPB is scanned with X-ray tomography method to provide geometrical reference of an actual foam. The sample is also integrated in a measurement cell to supply pressure loss data for the subsequent flow computations. For the second objective, pressure losses inside the RPB are measured for operations with and without foam packing to confirm the differences between the two operation modi and to provide comparative data for the CFD simulations.

2.1. X-ray tomography of the NCX1116 sample

The geometrical characteristics of the NCX1116 sample are examined as a 3D reconstruction through X-ray tomography method, providing void fraction and specific surface data of the foam for target values in the foam reconstruction step. The analysis process comprises of three steps. At first, 2000 projections of the foam sample are recorded over a range of 360° in order to calculate the X-ray absorption properties of the volume. For this purpose, a self-built setup consisting of a 150 kV microfocus X-ray source, a flat panel detector with a pixel size of 50 µm both from Hamamatsu and a rotation stage from Huber is used [35].

The distances between the source, detector and sample are selected so that the full sample fits inside the field of view leading to a magnification of 1.5 and thus an effective voxel size of 33 µm. The volume is reconstructed using the FDK algorithm [36] with the X-AID software from Mitos GmbH and the foam is segmented in Dragonfly 3D World from Comet from which a contour mesh was generated in Stereolithography (STL) format. The generated replica in the STL format is then analyzed using ParaView 5.8.0 [37] to obtain the porosity ϵ and the specific surface area a of the foam.

2.2. Pressure loss measurements of the NCX1116 sample

The same NCX1116 sample used in the geometrical characterization is also applied for the pressure loss measurements. As shown in Fig. 2, the sample has a length l of 54 mm in the streamwise direction and a width w of 57 mm. The height h of the sample is 10 mm. The sample is fixated inside a rectangular channel whose cross-sectional surface spans along the width and the height of the sample. At the inlet of the channel, a foam of the same type with a length of 20 mm is installed as a flow straightener. Structural measures through press-fitting of the metal foam sample into the rectangular channel are implemented to minimize potential flow bypass. Therefore, the measurement results are assumed to be unaffected thereof. However, it should be noted that such flow bypass cannot be quantified in our measurement setup.

During the experiment, the flow rate F and the pressure loss Δp are monitored at locations as schematized in Fig. 2. Pressure loss is measured using a differential pressure transmitter EJA110E from Yokogawa and the flowmeter Promag 53H from Endress+Hauser is used with specifications of respectively 0.055 % and 0.2 % accuracy. Water at temperature $\vartheta \approx 15\,^{\circ}\mathrm{C}$ is forced to flow through the porous sample while its flow rate is controlled by a valve. Unlike in the RPB operations, water is chosen as medium to obtain measurable pressure loss induced by the relatively small geometry of the foam sample. The measured flow rate is converted to the superficial velocity $U_s = \frac{F}{A_{\text{channel}}}$. The value pairs $\left(U_s, \frac{\Delta p}{l}\right)$ serve as validation data for the subsequent simulation.

Table 1
Specification of RPB experimental setup.

Item	Specification
Casing inner diameter	533 mm
Rotor outer diameter	450 mm
Metal foam inner/outer diameter/height	120 mm/190 mm/10 mm
Rotational speed	300 RPM, 900 RPM and 1500 RPM
Gas flow rate	9.66 $m^3\,h^{-1}$ and 28.9 $m^3\,h^{-1}$
Chemical system	1-propanol (for synthesis, ⩾ 95 %)
Pressure difference sensor	DeltaFox DMU 11 D AFRISO (0.91 % accuracy)

2.3. Experimental setup for the RPB

To reproduce the differences in pressure losses between two distinct operation modi, we performed experiments in the RPB in a cyclic process as shown in Fig. 3. The setup is a slight modification from [11] and is used due to practicality reasons. A summary of the specification is shown in Table 1. The vapor for the flow with 1-propanol (for synthesis, ⩾ 95 %) as medium is supplied through a kettle reboiler with 25 kW heat duty. It flows through the outer casing of the RPB, across the rotor, and leaves the RPB through the inner cavity. The vapor is then condensed completely before being pumped directly to the kettle reboiler. The coldest spot of the condenser is exposed to the atmosphere. The pressure difference is measured between the casing and the inner cavity of the RPB with a pressure transducers DeltaFox DMU 11 D from AFRISO with 0.91 % accuracy. The RPB unit is manufactured by Prospin sp. z o.o/Poland. Further details on the RPB unit can be found in [5,11].

As portrayed in Fig. 4 left, the rotor of the RPB consists of two interconnected metal disks with an outer diameter of 450 mm. The disks are separated by a 10 mm spacer where the packing can be fixated. The experiments are conducted in two different modes: with an annular metal foam packing NCX1116 from RECEMAT International inside the rotor and without packing between the disks. In the case where metal foam is used, the foam has an inner radius r_i of 60 mm and an outer radius $r_{p,o}$ of 95 mm as can be seen in Fig. 4 right.

The experiments themselves are conducted in the following manner. First, the kettle reboiler, the cooling water, and the pump are launched under a fixed rotational speed of the RPB. After a constant level in the kettle reboiler and a constant flow rate through the pump are reached, the rotational speed of the rotor is varied. Each rotational speed is maintained for 10 min, during which the pressure difference is recorded. This procedure is carried out for each gas flow rate and repeated three times for reproducibility.

3. Simulation setup

Following the experimental setup, we describe the numerical methods applied aiming to analyze the single-phase flow in the RPB locally. First, the reconstruction workflow of the metal foam will be introduced. The produced foam is subsequently verified through simulations corresponding to Section 2.2. Finally, the reconstructed foam is utilized in the flow computations of the RPB, corresponding to Section 2.3.

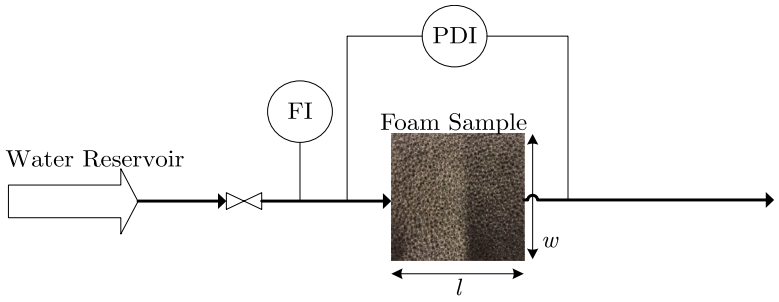

Fig. 2. Schematic setup for pressure loss measurement of the metal foam sample.

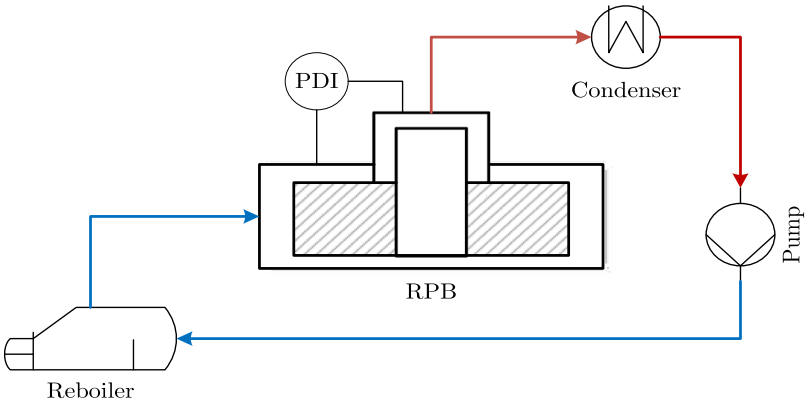

Fig. 3. Schematic setup for pressure measurements in the RPB.

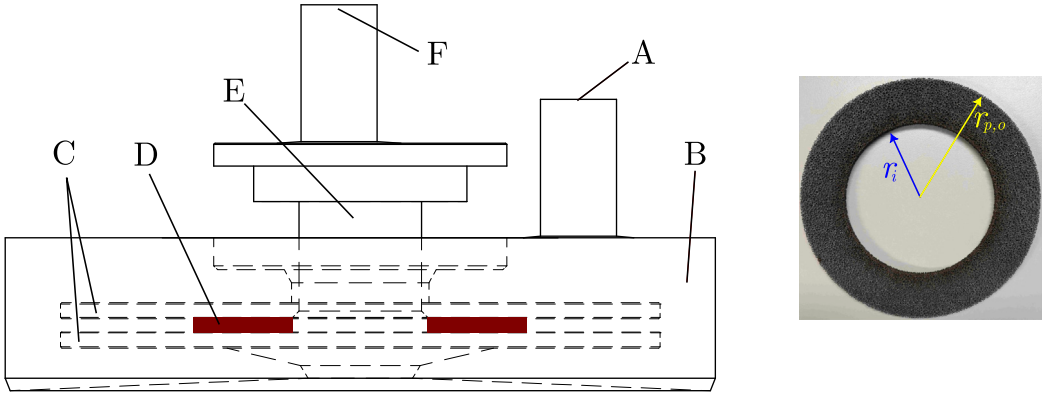

Fig. 4. Schematic drawing of the RPB (left) with the components: A - vapor inlet, B - casing, C - rotor, D - position of the metal foam packing, E - inner cavity, F - vapor outlet; and a picture of the annular metal foam (right) with its dimension.

3.1. Reconstruction workflow of metal foams

The metallic foam NCX1116 (see Fig. 4 right) commonly used as packing materials inside RPBs belongs to the category of open-cell solid foams. They consist of interconnected struts enclosing certain void regions, denoted as cells. The intersection point of the struts is called the node, whereas the hollow faces between two cells are called pores. These pores enable fluids to flow across the structure. Compared to other porous materials, open-cell foams possess distinguishable properties such as mechanical resistance, high porosity, large specific surface area, and high thermal conductivity, which make it attractive for heat and mass transfer processes.

In the past, several authors have opted for the reconstruction of the randomized open-cell model through scanning the foam using computed tomography methods and to use the subsequent digital reconstruction for further analysis [38]. This method has the apparent advantage of capturing actual foam characteristics. However, it is also limited to the availability of corresponding scanning device and to the size and resolution of the scanned data. Another option is the artificial reconstruction of the foam structure [33,34,39]. Unlike the computed tomography methods, no scanning devices are required. The resolution of the reconstructed foam also depends solely on the availability of computational resources. In this work, we opted for the artificial reconstruction method for two reasons: this method has been presented suitable to sufficiently capture characteristics of an actual foam, such as porosity, specific surface, and pressure loss. Moreover, this technique renders the necessity of scanning devices obsolete.

As presented by Bracconi et al. [34] and Agostini et al. [33], the reconstruction of the open-cell structure consists of three general steps. These steps are illustrated in Fig. 5. First, pore centers of the target foam structures are approximated through the sphere centers of a packing bed (Fig. 5 left). These coordinates become the foundation for the subsequent Voronoi tessellation algorithm to divide the space into polyhedrons that differ in sizes, in number of faces, and accordingly

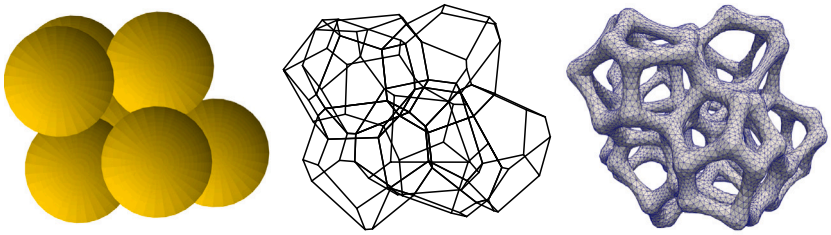

Fig. 5. Steps in the reconstruction workflow: generation of the sphere packing (left), Voronoi tessellation based on the sphere centers to produce the foam structure (middle), and solidification of the open-cell foam.

in number of edges. Fig. 5 in the middle shows the edges of such polyhedrons that resemble the structure of open-cell foams. The final step of the workflow is the solidification of the foam structure to model the actual geometry of the foam (Fig. 5 right).

The previously described reconstruction workflow is implemented as an in-house application written in C++. The generation of the sphere packing is based on a constructive algorithm presented by Lozano et al. [40]. The *Voronoi tessellation* step profits from the `voro++` library [41], which is a C++-library designed for handling large scale 3D Voronoi tessellations. To realize the three-dimensional solid structure, we utilize the `CGAL` library [42] to construct the nodes and the struts, to unite these individual entities as one solid representation, and subsequently to export the solid body as triangulated surface mesh. The main inputs of the application that influence the characteristics of the produced foam are the cell diameter d_C and the node diameter d_N. Through variations of these two variables, we performed a grid search to match the porosity ε and the specific surface area a between the reconstructed and the desired foam sample. The foams with characteristics close to the desired foam are further used in the simulations.

3.2. Simulation setup of the rectangular foam sample

Prior to applying the reconstructed metal foam for fluid flow simulation within the RPB, the reconstruction method described previously ought to be validated in a simpler flow setting. Therefore, the pressure loss from the complex flow through the metal foam is calculated and compared with measured data from the literature [34,43,44] or with the pressure loss measurement stated in the previous section.

A total of four samples are simulated for the validation of the reconstruction workflow. The porosity ε and specific surface a of the foam are either specified through the manufacturer or found in the literature. The fluid properties are set to match the experiments, which are air at temperature $\vartheta = 20\,°C$ for sample A and B, and water at temperatures $\vartheta = 20\,°C$ for sample "Recon-Mono" and $\vartheta = 15\,°C$ for sample "Recon-RPB", which will be further introduced in the discussion. The maximum empty tube velocity of all cases is $5\,m\,s^{-1}$. The velocities thus correspond to low Mach numbers (Ma < 0.3) and both air and water are assumed to be incompressible.

The flow calculation is carried out within the OpenFOAM v10 software framework [45,46]. A transient solver for isothermal and incompressible flow named `pimpleFoam` is chosen in accordance to the previously stated assumption. Possible turbulence in the flow is modeled using Reynolds-averaged Navier–Stokes (RANS) turbulence model $k\omega-$SST model by Menter and Esch [47] and Menter et al. [48] with low-Re wall treatment. The model is selected due to its versatility for both wall-bounded flows as well as free-stream turbulence.

The dimension of the domain for each case is defined as a subset of the actual dimension of the foam sample adopted for the experiments. Nevertheless, the size of the simulated domain is large enough to represent the full foam. Fully developed flow regime is acquired through cyclic boundary condition in the flow's streamwise direction and through symmetric boundary condition in the flow's crosswise direction. The surface of the foam is naturally described with wall boundary condition. The driving force of the flow is realized through a momentum source applied to all cells in the domain.

The meshes for the flow calculation are generated with the `snappyHexMesh` utility included in the OpenFOAM software. This utility automatically generates three dimensional meshes consisting of hexahedral and split-hexahedral cells from triangulated surface geometries in the STL format [46] provided in the foam reconstruction step. To accommodate the cyclic boundary condition, the computation domain must be mirrored in order to obtain correctly aligned faces between the two periodical boundaries. The resulting mesh as well as the foam as its boundaries is presented in Fig. 6.

3.3. Simulation setup for pressure loss calculation in the RPB

The verified foam reconstruction method is subsequently applied in the simulation inside the RPB to facilitate a more thorough flow analysis in the device. Naturally, the simulation of the RPB is set to mimic the corresponding experiments described in the previous section. The working fluid is 1-propanol in vapor form at $\vartheta = 97.5\,°C$. The parameters for the simulations can be taken from Table 1. It is assumed that the RPB is adiabatic, hence the fluid is isothermal and no phase change occurs inside the RPB. The flow is also assumed to stay in the range of low Mach number, which leads to the incompressibility of the fluid.

Similar to the experiments, the simulation also comprises the two operating modes, with and without foam packing inside the rotor. In the former case, the small pores of the metal foam must be resolved with computational cells with sizes significantly smaller than the casing and the inner cavity of the RPB domain. The resolution of the full annular form of the packing would require an enormous number of cells and is hitherto computationally unfeasible. Therefore, we reduce the computational domain into a 60°-slice of the equipment and utilize the cyclic boundary condition between the two corresponding sides (Fig. 7).

In details, the flow calculation inside the RPB domain is executed as follows. The geometry of the RPB is extracted from a 3D-model of the original equipment by isolating solely the surfaces of the equipment that come in contact with the fluid. We utilized the software suite SALOME 9.9.0 in this process. The extracted surfaces are subsequently triangulated with NETGEN [49], which is included within SALOME, and exported in the STL format. The surface data of the RPB serve as further input for the mesh generation process with `snappyHexMesh`. The flow computation is accomplished with the solver `pimpleFoam` within the OpenFOAM software framework. The flow's turbulent regime is modeled with the $k\omega-$SST model within the RANS approach with a single formula for the wall treatment [50]. The modeling of the rotating domain is realized by the Multiple Reference Frame (MRF) approach. The inlet of the RPB is assumed to be unaffected by the rotation and is defined as the proportional flow rate with regards to the full RPB.

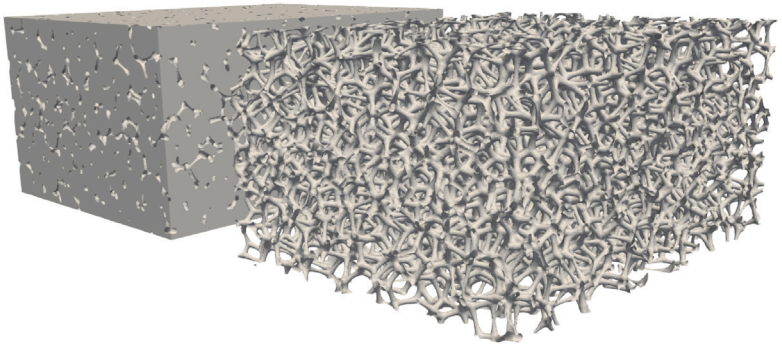

Fig. 6. Mesh for the pressure loss calculation generated with `snappyHexMesh` (left) from the open-cell foam produced by the reconstruction workflow (right).

Table 2
Geometrical parameters of Sample A and Sample B.

Sample	ε_{exp}	a (m^{-1})	ε_{sim}	a_{sim} (m^{-1})	ε_{error}	a_{error}	Source
A	0.897	649.0	0.874	648.66	2.564 %	0.052 %	Bracconi et al. [34]
B	0.862	1136.0	0.849	1129.25	1.508 %	0.594 %	Inayat et al. [43]

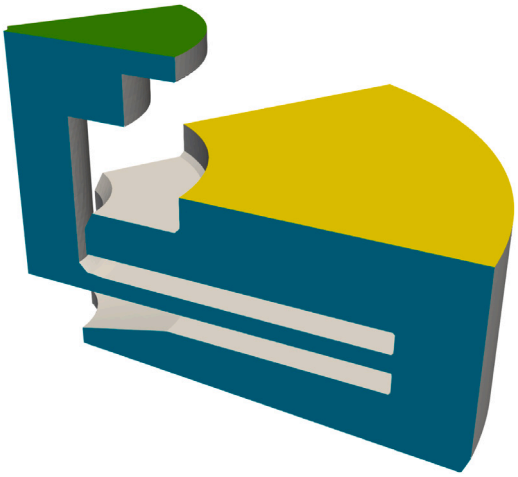

Fig. 7. Geometries of the sliced RPB with the inlet boundary (yellow face), outlet boundary (green face), cyclic boundary (turquoise face), and the inner solid walls of the RPB (gray faces).

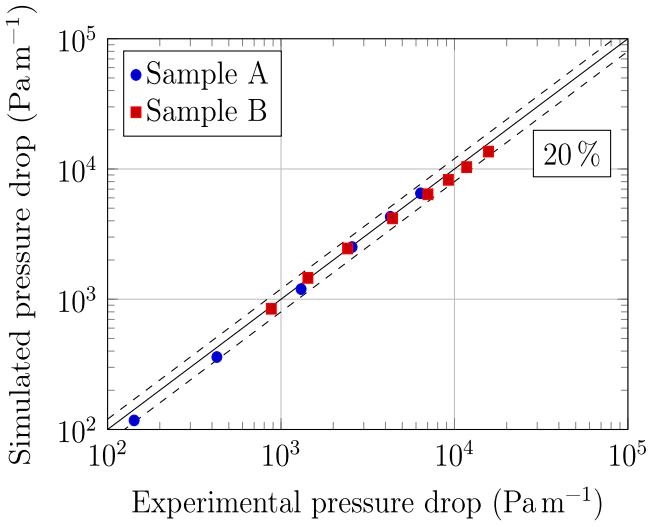

Fig. 8. Parity plot of experimental and simulated pressure loss for Sample A and B.

4. Results and discussion

The capability of the procedure presented in Section 3.1 to capture the correct transport phenomena is a crucial prerequisite for its use in the description of the metal foam packing inside the RPB. For this reason, the reconstructed foam structures are validated in a simpler flow configuration and these results are displayed first.

4.1. Validation of the reconstruction workflow

Two foam samples from the literature [34,43] are considered in the validation. Denoted as Sample A and Sample B, the geometrical parameters, namely the porosity ε and the foam's specific surface a, of the samples are shown in Table 2. In these regards, the deviations between the reconstructed foam and the reported experimental data are well below five percent relative error.

Aside from its geometrical properties, the reconstructed foams are also able to reproduce the transport characteristics of their corresponding counterparts in terms of pressure loss of the flow. The comparison of these pressure losses is displayed in Fig. 8. Overall, the simulated pressure losses have an error below 20 % relative to the experimental data. As reference, the reconstruction workflow presented by Bracconi et al. [34] showed relative errors of roughly 25 % or below.

Having demonstrated acceptable agreement of the reconstruction procedure to the two foam samples, we move on to the specific metal foam NCX1116 from RECEMAT International which is utilized as the RPB packing material. The manufacturer of the foam specifies a porosity ε of 0.92 and specific surface area a of 1000 m^{-1} for the said nickel-chromium foam. As reference for the validation, we include the geometrical properties of the foam through the X-ray scanning as well as both our pressure loss measurements and pressure loss data found in [44].

In terms of porosity ε and specific surface a, Table 3 shows the manufacturer's specification and the X-ray CT results labeled as "Scan-46M" and "Scan-74M". For the scanned data, their names reflect the number of points utilized to reconstruct the surface mesh in STL format. Interestingly, the X-ray CT scan shows lower porosity ε and higher specific surface area a, whereas the latter shows a relative difference above 50 %. Between the two scan results, the higher resolution in the surface mesh also corresponds to lower porosity and higher specific surface area. Through both the optical appearance of the foam and the surface mesh from the CT scan, we believe that these deviations are

Table 3
Geometrical parameters of the NCX1116 foam from technical data, CT-scan, and reconstruction workflow.

Source	ε	a (m^{-1})
Manufacturer's specification	0.92	1000
Scan-46M	0.894	1406.14
Scan-74M	0.889	1526.41
Recon-Mono	0.908	1263.52
Recon-RPB	0.865	1822.14

a product of cell compression close to the center of the foam's height. This compression has been observed by Gładyszewski et al. [23] as well and is most likely caused by mechanical stress during sheet rolling in the production process.

With the workflow described in Section 3.1, we generate two reconstructed foams. The first foam is labeled as "Recon-Mono" and is manufactured with sphere packing of constant diameter d_C. The second reconstructed foam is denoted as "Recon-RPB" and is generated to mimick the compression in the foam applied in the RPB experiments with polydisperse seeds in the reconstruction process. This is achieved through a distance function that places spheres with the smallest diameter at the center of the foam's height and increases the diameter as the spatial distance from the center rises. The geometrical properties of both reconstructed foams are also shown in Table 3. These properties differ from the specification from RECEMAT International, especially in the specific surface area a, where the relative discrepancy is larger than 20 % for Recon-Mono. In this case, we argue that the manufacturer's specification should only be considered as a rough reference. As stated by Calvo et al. [51], the electro-deposition technique for the manufacturing of nickel-chromium foam leads to a stochastic distribution of porosity and specific surface. Even if the foam in the study by Innocentini et al. [44] was not subjected to compression, its actual porosity and specific surface could in reality lie closer to reconstructed foam Recon-Mono. In the case of the reconstructed foam Recon-RPB, it exhibits an even lower porosity and a higher surface area than the X-ray scans. A possible explanation for these results is the fact that the outcome from the scanned foam depends strongly on the resolution of the scans, where current data suggests higher resolution would bring the porosity and the specific surface closer to our reconstructed foam.

The deviations in the geometrical properties of the foam are also reflected in the pressure loss comparison between our own experiment and the data from the literature [44]. This comparison is shown in Fig. 9 left. For similar range of superficial velocity U_s of the fluid up to $0.4\,m\,s^{-1}$, we observe higher pressure loss in our experiments compared to the literature data and we account for these differences on the following factors. On one hand, the flow of the fluid in our experiment is directed across the foam's height, as this is similar to the flow configuration inside the RPB. This particular flow direction results in a denser foam region at the center along the height and a more porous region for the rest of the foam. Due to this inhomogeneity, the local velocity of the fluid would be higher in the more porous region compared to a homogeneous foam, which in turn would increase the pressure loss. On the other hand, Innocentini et al. [44] did not report on any inhomogeneity in their foam sample, for which we could only assume that either their foam sample was not compressed or the fluid flowed in a direction where the compression would be less significant in their experiment.

We match the pressure loss from the CFD simulation with foam Recon-Mono to the experimental data reported in [44] in Fig. 9 right. The parity plot shows a good agreement in pressure loss, as the maximum deviation of the simulated pressure loss from the mean experimental data is around 18.5 %. The fact that our reconstructed foam with monodisperse seed matches the literature data supports the assumption of homogeneous foam in the literature data. Similarly, we compare the simulated pressure loss with foam Recon-RPB to our experimental pressure loss data in Fig. 9 right as well. Additionally, the simulated pressure loss with the scanned surfaces are also shown. The graph shows that for any given empty tube velocity, the simulated pressure losses with our reconstructed foam are closest to the experiments, followed by the simulation with Scan-74M and lastly Scan-46M. The first three experimental data points with lower velocity, and therefore lower pressure loss, are significantly underestimated by the simulations compared to the rest of data. However, it should be noted that the uncertainties of the experimental data for these points are also substantially higher than the rest. For the last four data points, the relative errors of the reconstructed foam lie well below 20 %, while the deviations from the scanned surfaces are higher. Relative errors in the range of 20 % are in similar order of magnitude as the reconstruction workflow presented in [34].

Considering these comparisons of geometrical properties and pressure loss, we believe that the reconstructed foam Recon-RPB matches our sample of NCX1116 foam applied in the RPB experiments. The results suggest that in general the implemented reconstruction procedure is able to capture the characteristics of the real foam. Moving forward, we use the settings applied for Recon-RPB for further simulations in the RPB.

4.2. Pressure measurements in the RPB

In conventional packed columns, the presence of packing material typically induces additional pressure loss due to friction in the system. However, the results from the experiments below insinuate otherwise. Fig. 10 presents the measured pressure differences between RPB's casing and RPB's eye for two different vapor flow rates and various rotor speeds. Regardless of empty or packed rotor, the measured pressure difference increases with increasing rotor speed. For each constant rotor speed, experiments with higher flow rates also exhibit higher pressure difference compared to their counterparts with lower flow rates. Remarkably, if we compare the experiments with empty rotor and experiments with packed rotor, the recorded pressure differences in operations with empty rotor are approximately twice as high as the records in operations with packed rotor. The disparities in pressures between empty and packed rotor are quite significant to be discarded as measurement errors, as shown by the error bands in Fig. 10. These error bands are calculated from the standard deviations of the three measurements in experiments of the same operating conditions.

Fig. 10 also shows direct comparison of the simulated pressure differences to the conducted experiments. This figure exhibits that the simulation results can reflect comparable fluiddynamic mechanism from the experiments, in particular that for a each gas flow rate and a certain rotational speed, the pressure loss of the operation mode without the metal foam is higher than the operation mode with packed rotor. However, in terms of absolute values, the calculated pressure differences from the simulations are always higher than the measured pressure loss from the experiments. The maximum relative error of 43.4 % is shown for operation with empty rotor, $F = 28.9\,m^3\,h^{-1}$, and $n = 1500$ RPM. We account for these errors on two factors. Firstly, the evaporation mode of the experiment means that the vapor is at its boiling point. This leads to unquantifiable condensation of n-Propanol inside the RPB. The condensed n-Propanol can act similar to lubricant for the vapor phase, exposing a slip boundary condition for the latter and possibly reduce the pressure loss compared to cases where the gas would not condense. Secondly, the simulation in the sliced domain of the RPB enforces an assumption for the inlet boundary condition that does not reflect the reality. In the experiments, the vapor is fed through a pipe at a non-centered point on the upper side of the casing. This cannot be realized in the sliced domain due to symmetrical condition and leads to more disparities in the pressure difference. Moreover, the discrepancies between the experiments and the simulations could stem from measurement errors on the experimental side as well as discretization errors on the simulation side. For the latter, we minimized

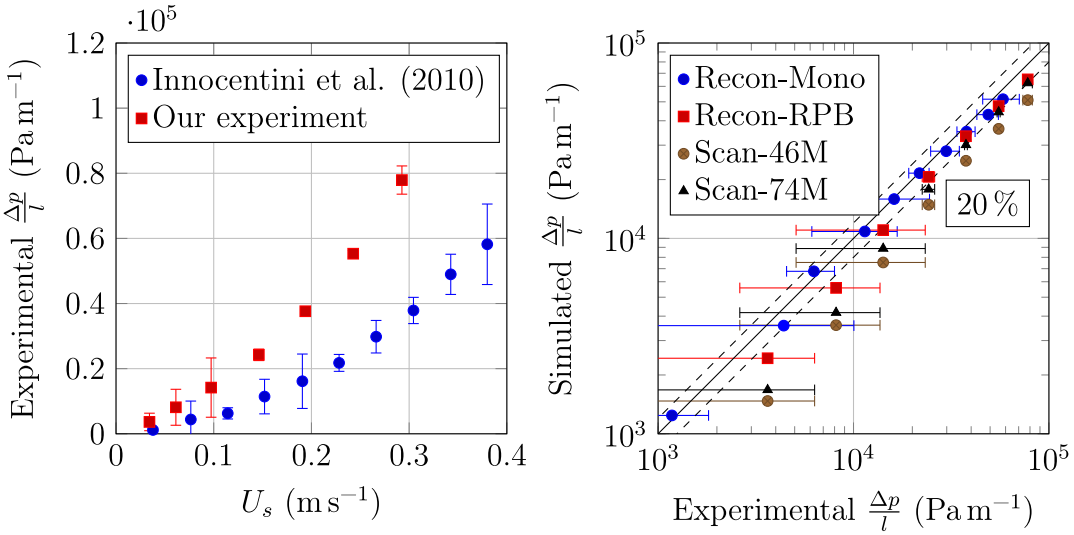

Fig. 9. Comparison of the experimental pressure loss over various superficial velocity between our experiments and literature data [44, left] and parity plot of experimental and simulated pressure loss (right).

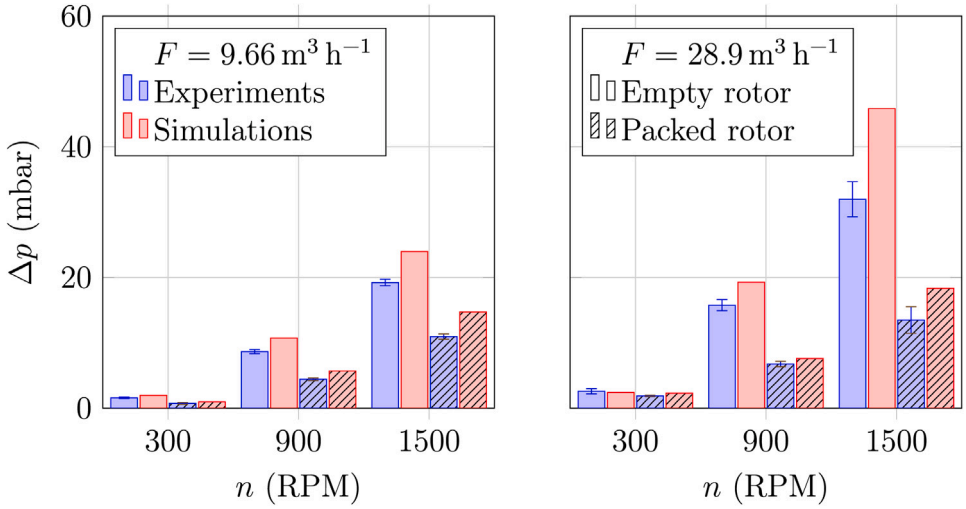

Fig. 10. Comparison of measured pressure differences between experiments and CFD simulations and between empty and packed rotor for $F = 9.66\,\mathrm{m^3\,h^{-1}}$ (left) and for $F = 28.9\,\mathrm{m^3\,h^{-1}}$ (right).

the discretization errors through a systematic mesh independent study reported in Appendix A. Regardless of these quantitative deviations between the experiments and the simulations, we consider the two data as comparable and the simulations are based on the correct underlying physics.

Therefore, we proceed with the discussion of the velocity profiles inside the RPB to reveal the differences between operations with empty and packed rotor. For this purpose, the velocities from the simulations are transformed into the cylindrical coordinates with the center of the RPB as the origin. Fig. 11 top presents the radial velocity U_r for the case with gas flow rate of $F = 28.9\,\mathrm{m^3\,h^{-1}}$ and a rotational speed of $n = 900\,\mathrm{RPM}$ along the radius of the rotor. Note that the gas flows inwards from the casing to the center of the RPB, which means that the fluid flows from right to left in the diagrams and the radial velocities are negative. The profiles of the radial velocity resemble the velocities resulting from the flow rate in consideration of the continuity. As the cross sectional area of the flow proportionally decreases with decreasing radius, the radial velocity increases following the relation in Eq. (1). In the case of operation with packed rotor, the jump at $r = 0.095\,\mathrm{m}$ in radial velocity is in accordance with the lower porosity ε of the metal foam, as the metal foam of the packed rotor has an outer radius of $r_{p,o} = 0.095\,\mathrm{m}$.

$$U_r = \frac{F}{\varepsilon\, 2\pi\, r\, h} \tag{1}$$

A rather remarkable results are shown in the azimuthal parts of the velocity, which are shown either as the tangential velocity U_φ in Fig. 11 middle or as the angular velocity ω_r in Fig. 11 bottom. As the gas enters the rotor section, it rotates in the same direction as the rotor as it previously gained the angular momentum through the outer part of the rotor in the casing. At first, the fluid rotates slower than the rotor, causing a momentum transfer from the rotor to the fluid and an acceleration of the fluid. At a point at roughly $r = 0.15\,\mathrm{m}$, the gas reaches the rotational speed of the rotor. However, the gas accelerates further as it flows inwards, where the tangential velocity reaches fourfold of the rotor's tangential velocity at the inner radius $r_i = 0.06\,\mathrm{m}$ for the case with empty rotor. Only when the metal foam is present will the fluid decelerate to the velocity of the rotor. Similar behaviors are observable in other flow rates and rotational speed in Fig. B.5.

The higher tangential velocities of the fluid compared to the rotor can be explained through the conservation of angular momentum.

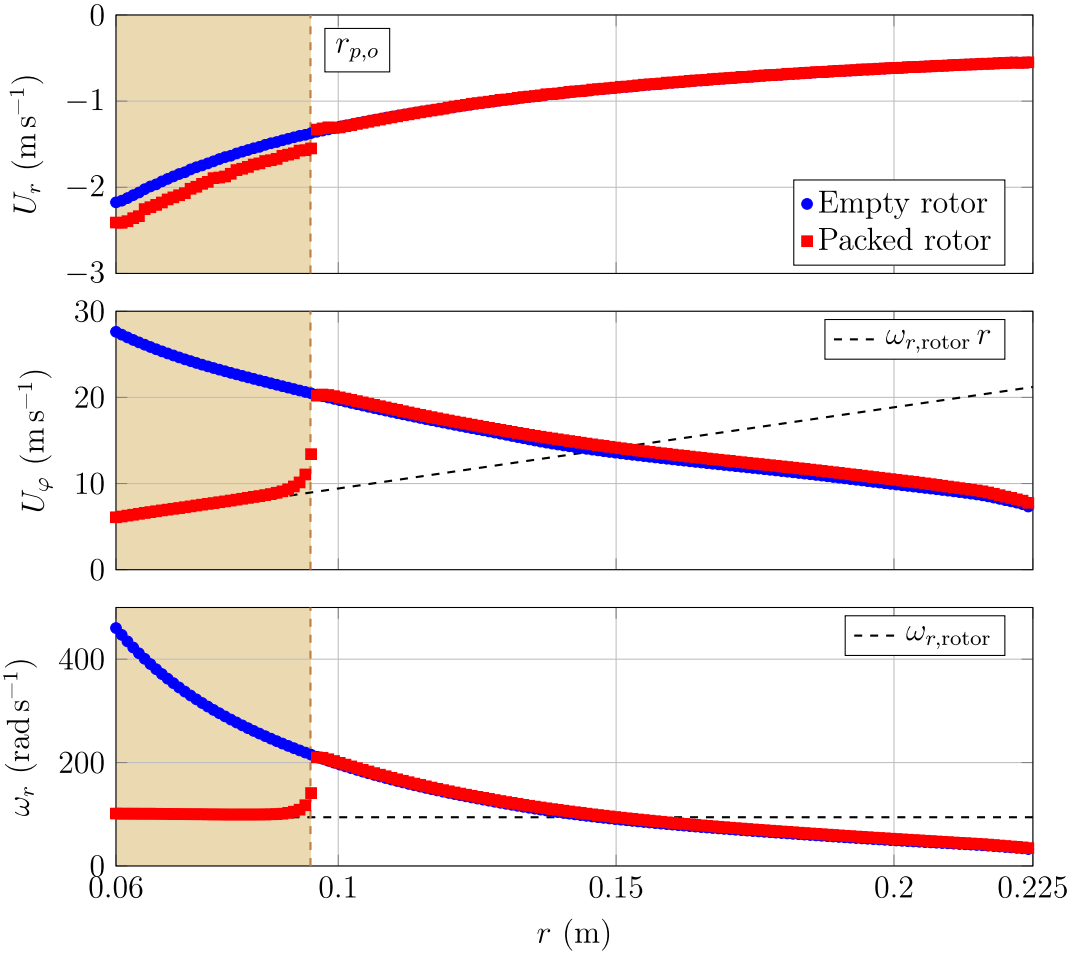

Fig. 11. Profiles of radial velocity U_r, tangential velocity U_φ, and angular velocity ω_r along the radius inside the rotor for $F = 28.9\,\text{m}^3\,\text{h}^{-1}$ and $n = 900\,\text{RPM}$ in the case of packed rotor, the metal foam spans from $r_i = 0.06\,\text{m}$ to $r_{p,o} = 0.095\,\text{m}$ on the vertical dashed brown line (brown background).

Without any external influences, a point of mass revolving around an arbitrary axis has a constant angular momentum L [52, Chapter 8.7]. When the fluid particle moves inwards in its orbit, the reduction of the distance to the axis is translated to an increase in angular velocity following Eq. (2). In the CFD simulations, momentum transfers from and to the rotor are taken into account. In the case of packed rotor, the drag between the metal foam and the fluid slows the fluid down into the rotational speed of the disk albeit the high porosity of the packing material. In the case of empty rotor, the friction between the fluid and the two rotor disks is not as high to decelerate the fluid.

$$L = m r^2\, \omega_r \tag{2}$$

In lights of these results, it is important to ask how the velocities and the pressure loss relate one to another. To answer this question, we define the total pressure in Eq. (3), neglecting the height difference in the equation. Differences in the total pressure represent the actual pressure loss, or in some cases, momentum gain. This is necessary, as the tangential acceleration of the fluid due to conservation of angular momentum described above would reduce the measured static pressure p, yet not necessarily an actual loss but merely energy conversion into kinetic energy.

$$p_\text{total} \equiv p + \frac{\rho}{2}\overline{\mathbf{U}} \tag{3}$$

The computation of the pressure loss will be classified into three segments. As depicted in Fig. 12, the first segment contains the casing, segment two represents the whole rotor from $r_i = 0.06\,\text{m}$ to $r_o = 0.225\,\text{m}$ independent of the presence of the metal foam, and the third segment is the RPB's center. These pressure losses are defined in Eqs. (4) to (6).

$$\Delta p_{\text{Segment 1}} = p_{\text{total, inlet}} - p_{\text{total},r_o} \tag{4}$$

$$\Delta p_{\text{Segment 2}} = p_{\text{total},r_o} - p_{\text{total},r_i} \tag{5}$$

$$\Delta p_{\text{Segment 3}} = p_{\text{total},r_i} - p_{\text{total, outlet}} \tag{6}$$

Fig. 13 shows the difference in average total pressure for the previously defined segments. In all data points, these differences show negative values for Segment 1, indicating that in the casing, the fluid gains more momentum from the rotor and accelerates in the direction of the rotor. In the second segment, the pressure loss in the packed rotor is actually higher than the pressure loss in the empty rotor. This suggests that the drag forces from metal foam are indeed higher than the friction force of the empty rotor, in accordance of common experience with other type of plants. Nevertheless, the friction in the empty rotor is also not negligible as the friction force is quadratically proportional to the velocity and the velocity in the empty rotor is significantly higher than the packed rotor. Finally, the pressure losses in the third segment are always higher in operations with empty rotor than the packed rotors. As the fluid reaches the center of the RPB, the circular movement of the fluid will be deflected into axial movement towards the outlet. In the process, fluid particles clash together and loose their momentum in form of drag force and eventually observable as pressure loss. As consequence, the high velocities in the operations with empty rotor translate into higher pressure loss.

The significance of the pressure loss in the inner cavity of a RPB is also visible from the effect of the gas flow rates on the measured pressure loss. Fig. 14 shows the experimental pressure differences between

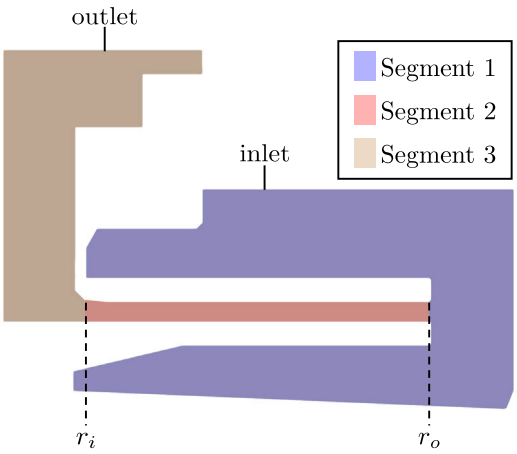

Fig. 12. Cross section of the RPB simulation setup to illustrate the segmentation for the computation of the pressure loss.

the inlet and outlet. The data are extended with experiments with metal foam packing spanning from $r_i = 0.06\,\text{m}$ to $r_o = 0.225\,\text{m}$, denoted as "Fully packed rotor". In this diagram, it is apparent that the flow rate has a more considerable effect on the pressure loss in operations without packing compared to the operations with packing. On one hand, the presence of the metal foam creates a drag on the gas flow and decelerates the gas to the rotational speed of the rotor tangentially as displayed in Fig. 11. Hence, the dynamic pressure loss in the inner cavity becomes more uniform and simultaneously less sensitive to the gas flow rate. Nevertheless, a higher gas flow rate induces higher radial velocity for the gas in the packing region and eventually slightly higher pressure loss due to the packing, which is also observable Fig. 14. The pressure loss induced by the packing is also visible in the comparison of packed bed with various length, where the pressure losses with "Fully packed rotor" are higher than experiments with "Packed rotor". Specific for $n = 1500\,\text{RPM}$, the pressure loss recorded for $F = 9.66\,\text{m}^3\,\text{h}^{-1}$ is slightly higher than the experiment with $F = 28.9\,\text{m}^3\,\text{h}^{-1}$, which could be explained with partial condensation of the fluid at high gas flow rate.

On the other hand, the drag induced by the two disks in the rotor (Segment 2) is not as substantial as the drag induced by the metal foam. As stated before, the gas could hence maintain its angular momentum and show tangential velocities much higher than the rotor itself. In the operations without packing, the difference between the two gas flow rates originates from inertia. The higher gas flow rate results in higher tendency of the gas to stay in motion or rather the drag induced by the disks becomes less efficient in decelerating the gas flow. Therefore, the gas exhibits higher tangential velocity upon leaving the rotor segment and undergoes higher pressure loss in the inner cavity, resulting in the sensitivity of the pressure loss on gas flow rates.

4.3. Note on turbulence inside the metal foam

As the simulations are conducted with the RANS turbulence model $k\omega-\text{SST}$, we are able to monitor the turbulence kinetic energy k along the radius of the rotor as a measure of turbulence level. The results of the turbulence kinetic energy from simulations with metal foam packing are shown in Fig. 15. The data show that in the range of radius $r = 0.06$ to $0.095\,\text{m}$, where the metal foam is located, the value of the turbulence kinetic energy is practically null. Similar observations can be conducted in viewing the turbulence intensity I, which is often referred to as turbulence level. The turbulence intensity is defined as the value of the mean turbulent velocity fluctuation U' relative to the mean velocity $\overline{U}$ (Eq. (7)).

$$I \equiv \frac{U'}{\overline{U}} = \sqrt{\frac{2k}{3\overline{U}^2}} \tag{7}$$

The corresponding turbulence intensity profiles are displayed in Fig. 16. Similar to Fig. 15, the turbulence level in the range of the metal foam's location is virtually zero. We argue that the small volumes of the foam's pores do not allow any formations of turbulence vortices. As a consequence, these observations remove the necessity of turbulence modeling in future multiphase simulations inside the metal foam packing.

According to Dybbs and Edwards [53], the Reynolds number for porous medium is defined as $\text{Re} = \frac{U_s(r)\,d_{\text{char}}}{\nu}$. In this definition, the superficial velocity U_s is defined as the total flow rate F divided by the cross-sectional area $2\pi r h$, where the latter changes along the radius of the rotor. The characteristic length d_{char} is equal to $0.445\,\text{mm}$, corresponding to the Sauter mean diameter or the sphere diameter with the same surface area to volume ratio of the metal foam. The kinematic viscosity of the fluid is denoted with ν. Although the fluid rotates along the RPB, the tangential velocity U_φ of the fluid is in this case insignificant, as the fluid is moving with roughly the same velocity as the packing, reducing the velocity difference $U_\varphi - \omega_{r,rotor} r$ to almost zero. For the two simulated flow rates $F = 9.66\,\text{m}^3\,\text{h}^{-1}$ and $28.9\,\text{m}^3\,\text{h}^{-1}$, the Reynolds numbers at the inlet of the metal foam packing $r_{p,o} = 0.095\,\text{m}$ are 41.0 and 122.6 respectively. At the inner radius $r_i = 0.06\,\text{m}$, where the velocity is the highest, the Reynolds numbers amount to 64.9 and 194.1. The approximated Re values fall in the category of laminar flow as defined by Dybbs and Edwards [53]. This supports the results of laminar flow regime shown in Fig. 16.

4.4. Discussion

The results of this investigation show that the counterintuitive behavior in pressure loss between operations with empty and packed rotor is explainable through the CFD simulations. It is also shown that the presence of metal foam reduces the tangential velocity of the fluid to the rotor's velocity. Albeit the constraints of smaller metal foam dimension in the rotor segment, the results of these study suggest following fundamental phenomena regarding the dry pressure loss. These underlying mechanisms should be considered in future development of pressure loss correlations for the RPB.

In the casing or in the outer cavity of the RPB, the gas is not subjected to any pressure loss. On the contrary, the gas would gain momentum through the rotation of the rotor and would accelerate tangentially as indicated by the negative total pressure difference for Segment 1 in Fig. 13. This observation confirms the statement by Neumann et al. [15] that the rotor acts as a compressor in the outer cavity. We therefore suggest that the outer cavity of the RPB does not have any contribution to the pressure loss. This finding raises the question if such behavior is also observable when the rotor is fully packed with the metal foam. With the metal foam, the cross sectional area at rotor's outer radius will be narrowed down by a factor of the foam's porosity which causes higher friction as the fluid enters the rotor. However, the presence of the foam will accelerate the fluid flow in the tangential direction, leading to higher momentum gain of the fluid. We believe that the momentum gain outweighs the friction, so that the contribution to pressure loss in the outer cavity remains negligible. To be fair, this assumption should be verified with CFD simulations with packing that spans over the whole radius of the rotor in the future.

In the rotor segment, the small pores of the metal foam as packing material would result in laminar flow of the gas. This would suggest that the pressure loss induced in this segment would be linear to the gas velocity since the pressure loss is proportional to velocity in laminar flow regime. Correlations for dry pressure loss in this segment should

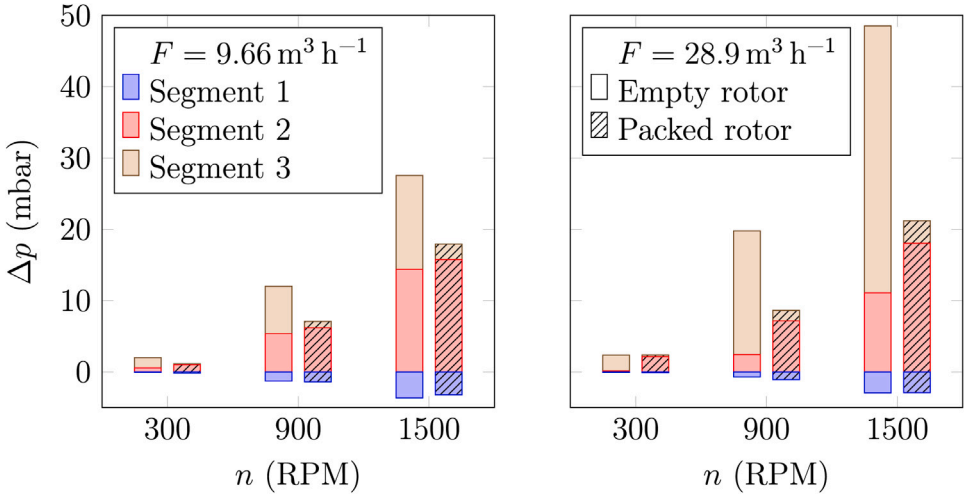

Fig. 13. Average total pressure difference at different segments inside the RPB. For each rotational speed n and each flow rate F, the left solid bar shows the empty rotor mode and the right striped bar shows the packed rotor mode.

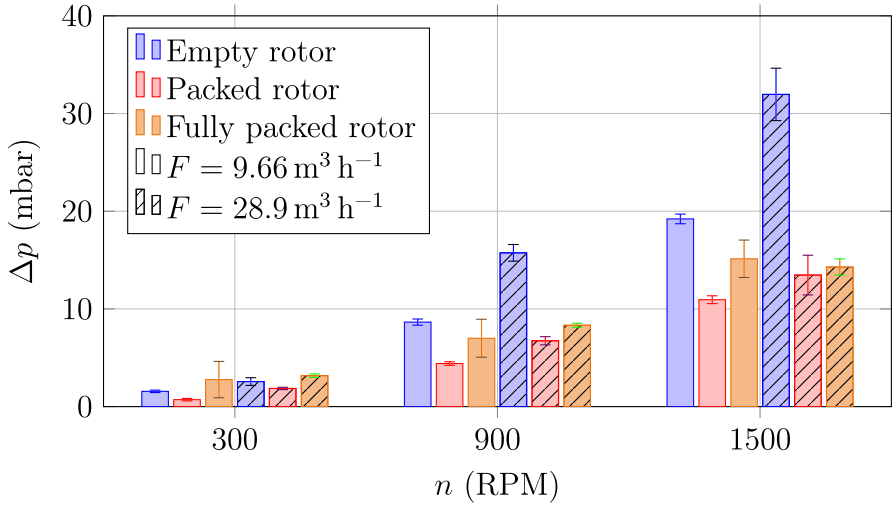

Fig. 14. Experimentally measured pressure differences between inlet and outlet for RPB with and without packing under different flow rates F and rotational speed n.

thus include a proportionality of the pressure loss to the velocity (see Eq. (8)).

$$\Delta p_{\mathrm{rotor}} \propto \frac{F}{A} \tag{8}$$

Lastly, the inner cavity of the RPB, often referred to as the "eye", poses a significant share in form of dynamic pressure loss. It can therefore be speculated, that the pressure loss in this sector is proportional to the squared mean velocity of the fluid upon leaving the rotor segment as shown in Eq. (9). The mean fluid velocity could be approximated as the superficial fluid velocity from the fluid flow rate radially U_r and the tangential velocity of the rotor U_φ at the inner radius of the packing r_i.

$$\Delta p_{\mathrm{eye}} \propto \overline{U}^2 = \sqrt{U_r^2 + U_\varphi^2} \tag{9}$$

We attempt to illustrate the proportionality in Eq. (9) in Fig. 17. The figure shows the pressure loss in the inner cavity for each fluid flow rate upon variation of the rotational speed, resulting in the various squared mean fluid velocity $\overline{U}^2$. Regardless of the sparse availability of the data, the three data points for each flow rate could show the linear relation between the two parameters qualitatively.

This study suggests that reducing the inner radius of the rotor while maintaining the bed length could reduces the pressure loss. On one hand, the presence of the metal foam packing does not have significant influence on the radial velocity U_r as visualized in Fig. 18 left. On the other hand, Fig. 18 right shows the notable difference in tangential velocity U_φ due to the packing. As higher tangential velocity induces higher pressure loss and the tangential velocity of the fluid takes on the velocity of the rotor, decreasing the inner radius would lead to a reduction of pressure loss. However, for actual RPB operations, the liquid phase must be taken into account and the reduction of the inner radius is only practicable to a certain degree. Structurally, the inner radius of the packing is limited to the size of the liquid distributor, which is positioned in the inner cavity at the height of the packing. Furthermore, the packing must accelerate the liquid radially outwards. Reduced inner radius of the packing would cause flooding more susceptible and therefore reduce the operational window of the RPB. A more detailed look into the pressure loss with the addition of liquid phase would be interesting in the future, as we believe that the presence of liquid in the inner cavity would also alter the tangential velocity and ultimately the pressure loss.

The results of this section would also explain the generally higher pressure loss in HiGee-plants with different packing types, such as the Rotating Zigzag Bed (RZB). For future correlation developments, we discourage the analogy to conventional packed column, where the total pressure loss in the RPB is the summation of the contribution of the empty rotor and the contribution of the packing material [see e.g. 15].

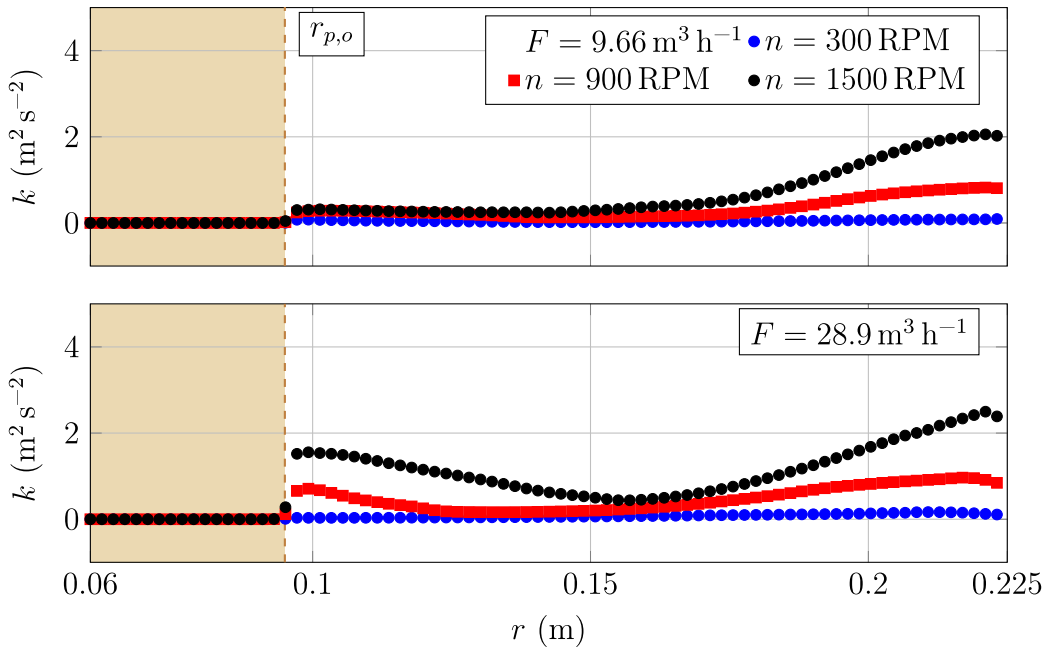

Fig. 15. Profiles of turbulent kinetic energy k along the radius inside the rotor with the presence of the metal foam spans from $r_i = 0.06\,\mathrm{m}$ to $r_{p,o} = 0.095\,\mathrm{m}$ on the vertical dashed brown line (brown background).

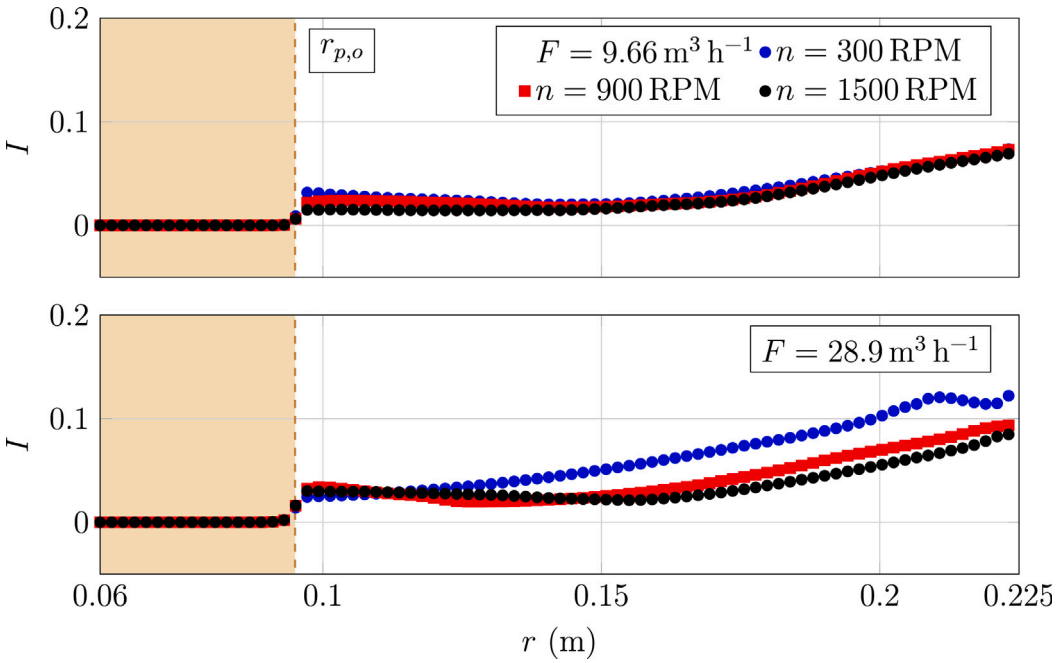

Fig. 16. Profiles of turbulence intensity I along the radius inside the rotor with the presence of the metal foam spans from $r_i = 0.06\,\mathrm{m}$ to $r_{p,o} = 0.095\,\mathrm{m}$ on the vertical dashed brown line (brown background).

We suggest instead a simplification of the Navier–Stokes (NS) equations in the radial direction to account for changes in radial and tangential velocities of the flow to the pressure loss.

5. Conclusion and outlook

The purpose of this study is to present the counterintuitive behavior regarding the pressure loss in RPB experiments as well as the explanation through CFD simulation results. The experiments show that the dry pressure drop in operations without packing materials exceeds the recorded pressure losses in operations with metal foam packing. This is contrary to common experiences with conventional packed bed columns, as the presence of packing material usually contributes to higher pressure loss.

However, evidence from the simulations suggests that there are two distinct phenomena which must be taken into account in pressure drop consideration inside RPBs. On one hand, fluids that undergo rotational motion on a certain axis while flowing radially inwards must maintain their angular momentum. Therefore, they would rotate faster towards the center and contribute to a higher dynamic pressure loss. On the other hand, the presence of metal foam indeed induce more drag and hence increased pressure loss. Nevertheless, the dynamic pressure loss

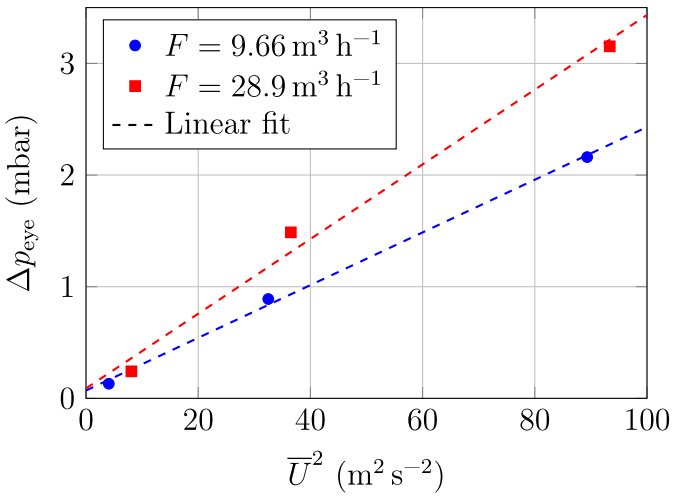

Fig. 17. Proportionality of the pressure loss in the inner cavity to the squared mean velocity in operations with packed rotor.

in operations without metal foam exceeds the pressure drop through drag in the packing material for the specific RPB geometry used in this study, leading to the seemingly paradoxical behavior.

In real applications, it is actually nonsensical to operate the RPB with empty rotor. The packing induces dispersion in the liquid for higher interfacial area in the device, which is desirable for heat and mass transfer. However, this work contributes in extending our knowledge on the fluid dynamics inside the RPB. The results show the significance of the azimuthal part of the fluid flow and its consequences on the dynamic pressure loss. The data acquired from this investigation and the derived proportionalities between gas flow rate and pressure drop could inspire in the enhancement of existing correlations regarding the pressure loss in RPB.

Further, we successfully implement the virtual reconstruction workflow of the metal foam from the literature for CFD simulations. The reconstructed foam is not only validated in simpler cases with single-phase translational flow, but also under the rotational motion of the fluid in the RPB. This technique is more flexible than experimental reconstruction of the foam through computed tomography as it can be easily applied for a wider range of foam dimension, limited only by computational resources and not by the scanner capability. Apart of its usage in the RPB simulations, the implemented workflow could also be useful in the study of porous materials in connection with its fluiddynamic and heterogeneous catalytic reactions.

Moving forward, we would utilize the foam reconstruction as well as the CFD workflow with resolved metal foam packing for simulative studies of gas–liquid flow in the RPB. Using interface resolving multiphase simulation framework, we will be able to describe the gas–liquid–solid interaction as well as the flow morphologies and to predict the effective surface area between gas and liquid *a priori* of any measurements. These insights will complement the current knowledge of the multiphase flow and provide correlations for more accurate process models of the RPB.

CRediT authorship contribution statement

Felix Febrian: Writing – original draft, Visualization, Methodology, Investigation, Conceptualization. **Georg Brösigke:** Writing – review & editing, Supervision, Project administration, Methodology, Conceptualization. **Paul H. Kamm:** Writing – original draft, Investigation. **Jens-Uwe Repke:** Writing – review & editing, Funding acquisition, Conceptualization.

Funding

The authors declare no competing financial interest.

Declaration of competing interest

The authors declare that they have no known competing financial interests or personal relationships that could have appeared to influence the work reported in this paper.

Acknowledgment

The authors thank Jakob Luis Köntopf and Dietmar Plotka for their assistance and support.

Appendix A. Mesh refinement studies

The simulations reported in this work are subjects to prior mesh refinement studies. Fig. A.1 shows the refinement study of Sample A for the pressure drop simulations of the flow inside the reconstructed foam. The mesh refinement is accomplished through reducing the cell size of the base mesh, which is the input for the utility `snappyHexMesh`. For the quantification of the computational efforts, the average cell length δ of the numerical meshes is used instead of the absolute number of cells N. The average cell length is given as

$$\delta = \sqrt[3]{\frac{V}{N}}, \tag{A.1}$$

where V is the total volume of the numerical domain. This value is applied to accommodate the various characteristics of the samples.

The mesh refinement study for Sample A employs a total of four different mesh sizes. The resulting pressure drop is shown as blue bars corresponding to the left axis and the average cell length is shown as red circles corresponding to the right axis in Fig. A.1. Compared to calculations with the finest mesh, the simulations with mesh refinement levels one to three have a relative difference of 5.45 %, 3.23 % and 0.7 % in pressure drop respectively. From these results, the mesh refinement level two can already achieve an error of below %. For this reason, the numerical meshes are generated with average cell length of $\delta \leqslant 1 \times 10^{-4}$ m in further simulations with the rest of the foam samples, which is consistent to the refinement level two in Fig. A.1.

Similar to the refinement study for the reconstructed foam, the different sizes for the mesh in the RPB simulation are acquired through the variation of the base mesh for `snappyHexMesh`. Fig. A.2 presents the results for the mesh convergence for the RPB with an empty rotor, a gas flow rate of $F = 28.9\,\mathrm{m^3\,h^{-1}}$, and rotational speed of $n = 900$ RPM. In this case, five different mesh sizes are compared with the pressure difference between the inlet and outlet of the RPB as reference value.

As before, the deviation of the pressure loss of the first four meshes are calculated relative to the result of the finest mesh. In the order of the meshes from one to four, the relative deviations amount to 8.19 %, 7.17 %, 1.41 % and 2.94 % accordingly. It is apparent, that the mesh with refinement level three is sufficient to achieve a low discretization error and the mesh setting is thus utilized for further simulations.

Further, we also employ this particular mesh settings for the simulations of the RPB with packed rotor. The assumption is that the presence of the metal foam would only alter the flow at the vicinity of the foam, ergo only the mesh refinement level around the metal foam must be further investigated. We created three different mesh refinement levels that are shown in Fig. A.3.

Compared to the finest mesh, the relative deviations in pressure difference between the inlet and outlet of the RPB amount to 14.78 % for the mesh with refinement level one and 2.54 % for mesh with refinement level two. In the latter setting, the produced mesh has an average cell length of $\delta \approx 1 \times 10^{-4}$ m in the vicinity of the reconstructed foam, which is consistent with the mesh convergence study of the isolated foam sample in Fig. A.1. The mesh with refinement level two in Fig. A.3 is used in further simulations.

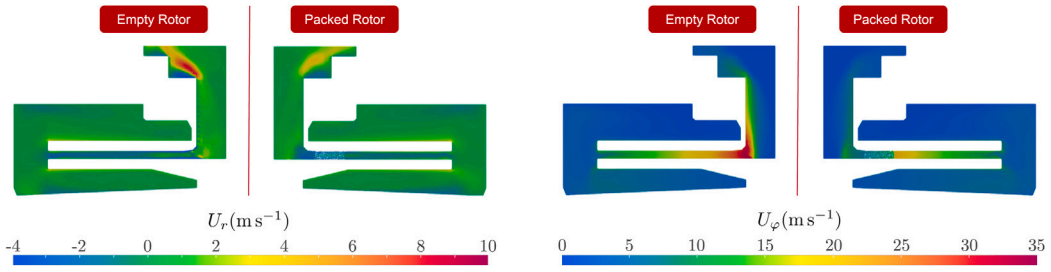

Fig. 18. Comparison of the radial velocity U_r (left) and the tangential velocity U_φ (right) on a cross-section of the RPB between empty and packed rotor operations for $F = 28.9\,\mathrm{m^3\,h^{-1}}$ and $n = 900\,\mathrm{RPM}$.

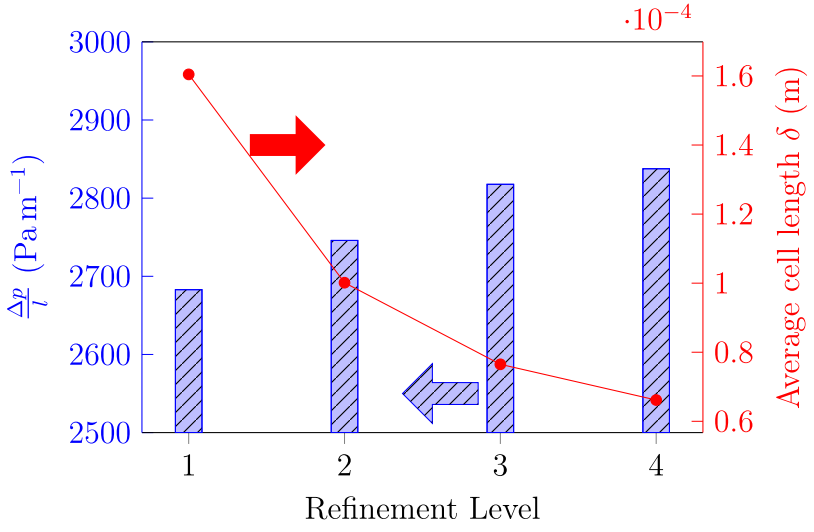

Fig. A.1. Mesh refinement study for simulation with Sample A, empty tube velocity $U_s = 3\,\mathrm{m\,s^{-1}}$.

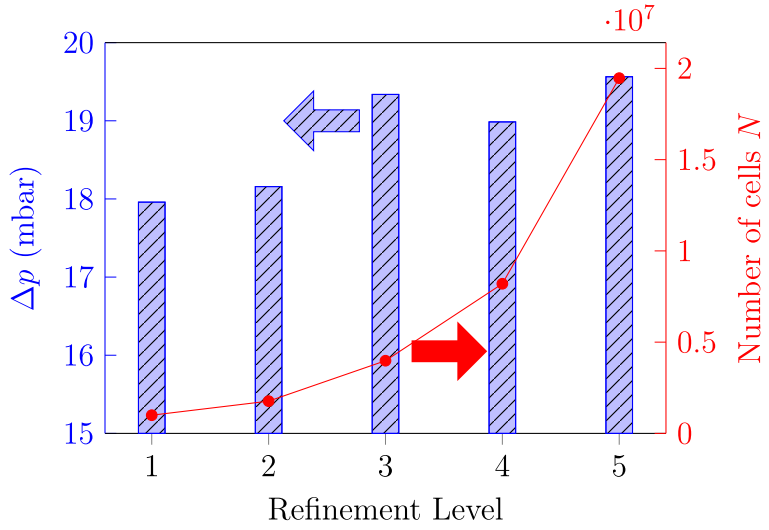

Fig. A.2. Mesh refinement study for RPB simulation with empty rotor, $F = 28.9\,\mathrm{m^3\,h^{-1}}$, $n = 900\,\mathrm{RPM}$.

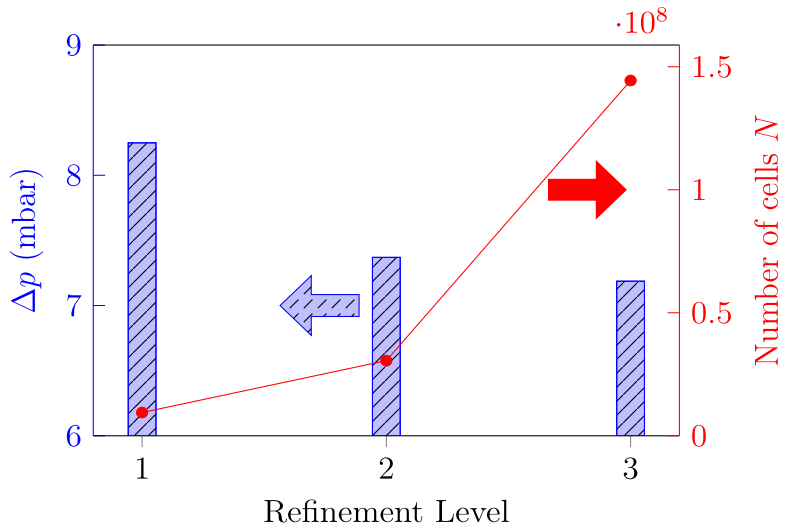

Fig. A.3. Mesh refinement study for RPB simulation with packed rotor, $F = 28.9\,\mathrm{m^3\,h^{-1}}$, $n = 900\,\mathrm{RPM}$.

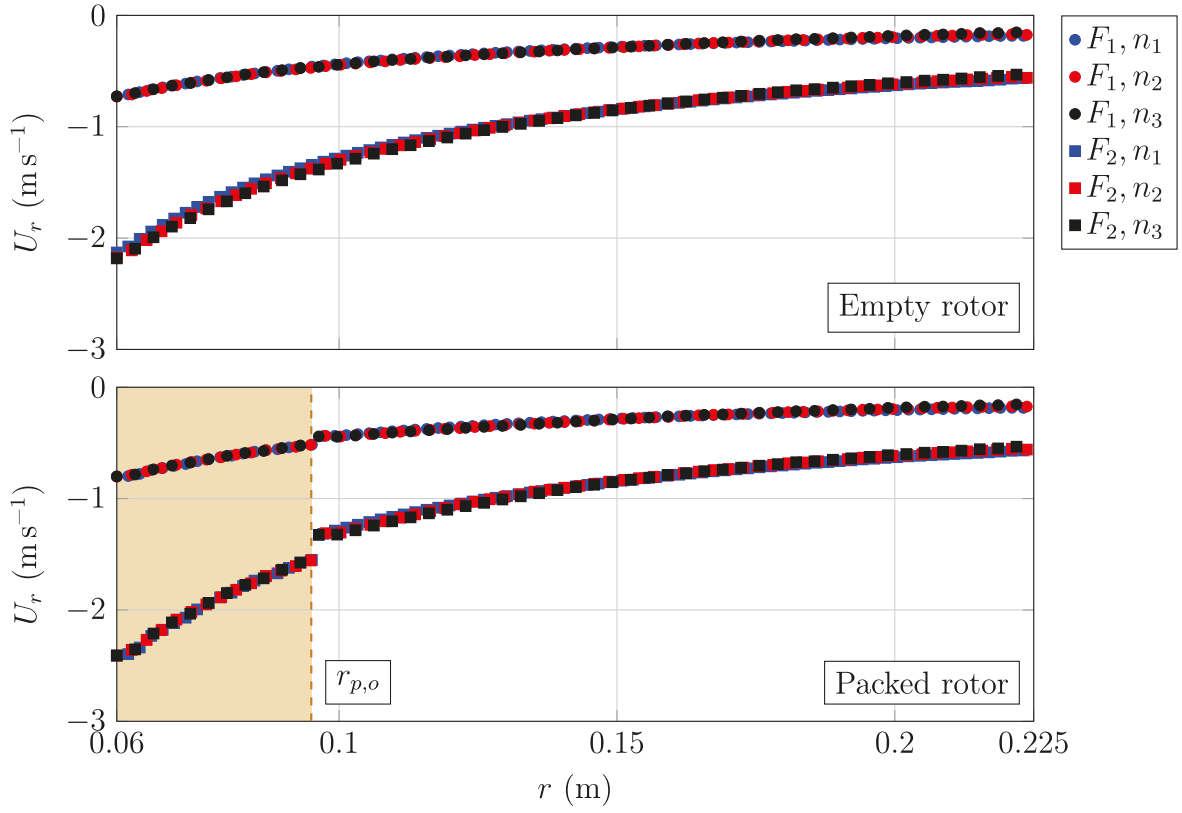

Fig. B.4. Profiles of the radial velocities U_r along the radius inside the rotor for operations with empty rotor (top) and packed rotor (bottom). In the packed rotor case, the metal foam spans in the brown area.

Appendix B. Velocity profiles in the rotor

The behavior of the gas flow displayed in Fig. 11 can also be recovered from the simulations with different gas flow rates F and rotational speed n as shown in Fig. B.4 for the radial velocities U_r and in Fig. B.5 for the tangential velocities U_φ. The notations for the legends are as follow: $F_1 = 9.66\,\mathrm{m^3\,h^{-1}}$, $F_2 = 28.9\,\mathrm{m^3\,h^{-1}}$, $n_1 = 300\,\mathrm{RPM}$, $n_2 = 900\,\mathrm{RPM}$, and $n_3 = 1500\,\mathrm{RPM}$.

On one hand, it is apparent in Fig. B.4 that the radial velocity U_r of the gas flow is dependent mainly on the gas flow rate F. This dependency follows the relation shown in Eq. (1). The presence of the metal foam in the brown area in Fig. B.4 bottom influences the radial velocity through lower porosity ε.

On the other hand, the tangential velocity U_φ mainly depends on the rotational speed n based on Fig. B.5. Higher rotational speed of the RPB accelerates the fluid at the inlet of the rotor, which means the fluid has higher angular momentum that has to be conserved as the fluid flows inwards, resulting in even higher tangential velocity (see Eq. (2)). Fig. B.5 also displays the influence of the flow rate on the tangential velocity. In the span between $r = 0.06\,\mathrm{m}$ to $r = 0.125\,\mathrm{m}$, the top figure in Fig. B.5 shows that higher flow rate causes higher inertia

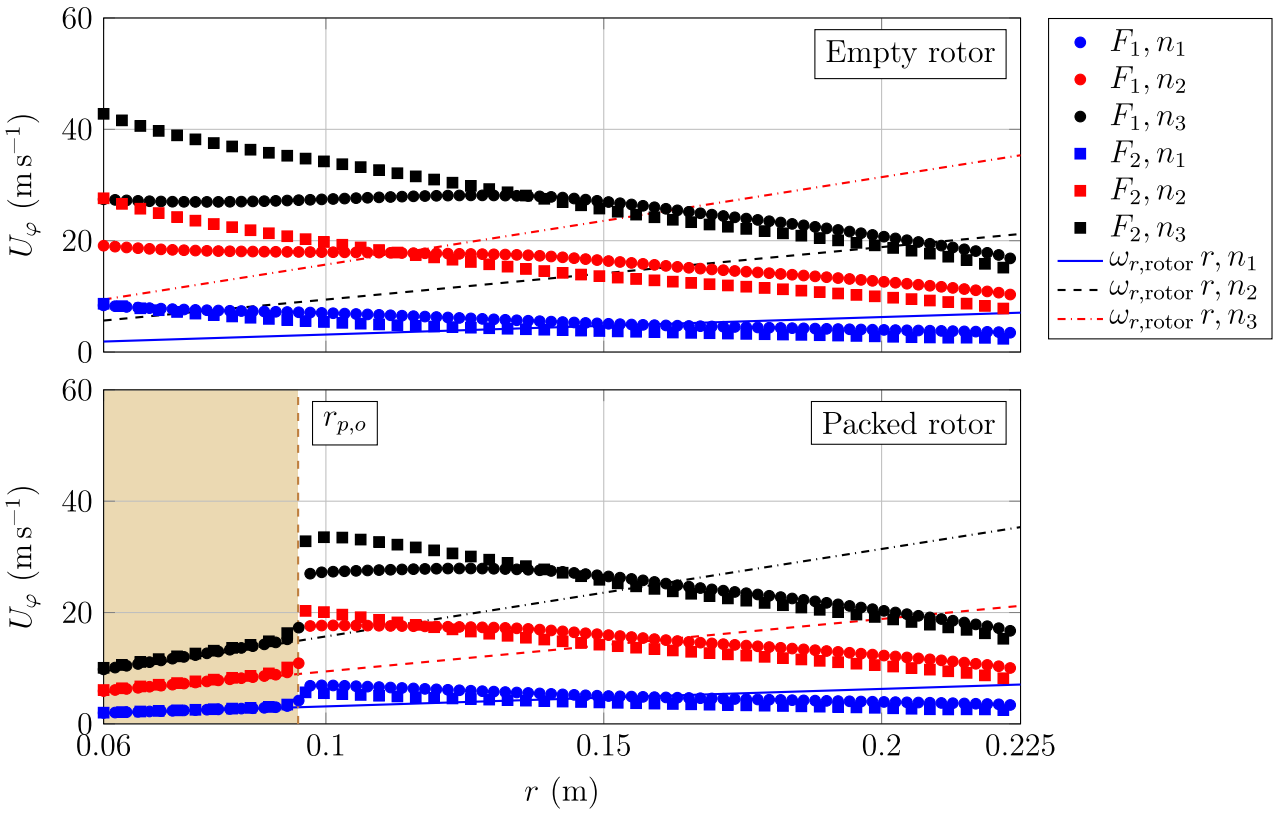

Fig. B.5. Profiles of the tangential velocities U_φ along the radius inside the rotor for operations with empty rotor (top) and packed rotor (bottom). In the packed rotor case, the metal foam spans in the brown area. The lines denote the rotor's velocity.

of the fluid, leading to less deceleration of the flow due to friction with the rotating disk of the rotor.

Data availability

Data will be made available on request.

References

[1] H. Zhao, L. Shao, J.-F. Chen, High-gravity process intensification technology and application, Chem. Eng. J. 156 (3) (2010) 588–593, http://dx.doi.org/10.1016/j.cej.2009.04.053.

[2] G.E. Cortes Garcia, J. Van Der Schaaf, A.A. Kiss, A review on process intensification in HiGee distillation, J. Chem. Technol. Biotechnol. 92 (6) (2017) 1136–1156, http://dx.doi.org/10.1002/jctb.5206.

[3] K. Neumann, K. Gladyszewski, K. Groß, H. Qammar, D. Wenzel, A. Górak, M. Skiborowski, A guide on the industrial application of rotating packed beds, Chem. Eng. Res. Des. 134 (2018) 443–462, http://dx.doi.org/10.1016/j.cherd.2018.04.024.

[4] M. Skiborowski, A. Górak (Eds.), Process Intensification: By Rotating Packed Beds, second ed., De Gruyter, Boston, 2022.

[5] M. Hilpert, G.U. Calvillo Aranda, J.-U. Repke, Experimental analysis and rate-based stage modeling of multicomponent distillation in a rotating packed bed, Chem. Eng. Process. - Process. Intensif. 171 (2022) 108651, http://dx.doi.org/10.1016/j.cep.2021.108651.

[6] A. Ressemann, M. Illner, J.-U. Repke, Local separation performance for distillation processes in rotating packed beds: transferability and applicability, Ind. Eng. Chem. Res. 63 (30) (2024) 13291–13307, http://dx.doi.org/10.1021/acs.iecr.4c01422.

[7] Y.-S. Chen, Correlations of mass transfer coefficients in a rotating packed bed, Ind. Eng. Chem. Res. 50 (3) (2011) 1778–1785, http://dx.doi.org/10.1021/ie101251z.

[8] M. Hilpert, J.-U. Repke, Experimental investigation and correlation of liquid-side mass transfer in pilot-scale rotating packed beds, Ind. Eng. Chem. Res. 60 (14) (2021) 5251–5263, http://dx.doi.org/10.1021/acs.iecr.1c00440.

[9] J. Koop, N. Bera, E. Quickert, M. Schmitt, M. Schlüter, C. Held, G. Schembecker, Separation of volatile organic compounds from viscous liquids with RPB technology, Ind. Eng. Chem. Res. 62 (34) (2023) 13637–13645, http://dx.doi.org/10.1021/acs.iecr.3c01597.

[10] P.-J. Liang, D.-C. Cheng, H.-Y. Xu, C.-y. Xu, G.-W. Chu, H.-K. Zou, B.-C. Sun, J.-F. Chen, Simultaneous absorption of H2S, MM and COS into a novel SRSG absorbent using a rotating packed bed, Sep. Purif. Technol. 346 (2024) 127374, http://dx.doi.org/10.1016/j.seppur.2024.127374.

[11] A. Ressemann, M. Illner, J.-U. Repke, A methodology for the analysis of distillation processes within rotating packed beds based on local temperature measurements, Chem. Eng. Res. Des. 193 (2023) 198–206, http://dx.doi.org/10.1016/j.cherd.2023.03.018.

[12] H. Qammar, T. Pyka, J. Koop, A. Górak, G. Schembecker, Radial temperature profile measurements to understand mass transfer in rotating packed bed distillation, Ind. Eng. Chem. Res. 62 (38) (2023) 15588–15599, http://dx.doi.org/10.1021/acs.iecr.3c01068.

[13] H.-S. Liu, C.-C. Lin, S.-C. Wu, H.-W. Hsu, Characteristics of a rotating packed bed, Ind. Eng. Chem. Res. 35 (10) (1996) 3590–3596, http://dx.doi.org/10.1021/ie960183r.

[14] C. Zheng, K. Guo, Y. Feng, C. Yang, N.C. Gardner, Pressure drop of centripetal gas flow through rotating beds, Ind. Eng. Chem. Res. 39 (3) (2000) 829–834, http://dx.doi.org/10.1021/ie980703d.

[15] K. Neumann, S. Hunold, M. Skiborowski, A. Górak, Dry pressure drop in rotating packed beds—systematic experimental studies, Ind. Eng. Chem. Res. 56 (43) (2017) 12395–12405, http://dx.doi.org/10.1021/acs.iecr.7b03203.

[16] T. Pyka, J. Koop, C. Held, G. Schembecker, Dry pressure drop in a two-rotor rotating packed bed, Ind. Eng. Chem. Res. 61 (46) (2022) 17156–17165, http://dx.doi.org/10.1021/acs.iecr.2c02500.

[17] J.R. Burns, C. Ramshaw, Process intensification: Visual study of liquid maldistribution in rotating packed beds, Chem. Eng. Sci. 51 (8) (1996) 1347–1352, http://dx.doi.org/10.1016/0009-2509(95)00367-3.

[18] K. Guo, F. Guo, Y. Feng, J. Chen, C. Zheng, N.C. Gardner, Synchronous visual and RTD study on liquid flow in rotating packed-bed contactor, Chem. Eng. Sci. 55 (9) (2000) 1699–1706, http://dx.doi.org/10.1016/S0009-2509(99)00369-3.

[19] A. Bašić, M.P. Duduković, Liquid holdup in rotating packed beds: Examination of the film flow assumption, AIChE J. 41 (2) (1995) 301–316, http://dx.doi.org/10.1002/aic.690410212.

[20] J.R. Burns, J.N. Jamil, C. Ramshaw, Process intensification: operating characteristics of rotating packed beds — determination of liquid hold-up for a high-voidage structured packing, Chem. Eng. Sci. 55 (13) (2000) 2401–2415, http://dx.doi.org/10.1016/S0009-2509(99)00520-5.

[21] Y. Yang, Y. Xiang, G. Chu, H. Zou, Y. Luo, M. Arowo, J.-F. Chen, A noninvasive X-ray technique for determination of liquid holdup in a rotating packed bed, Chem. Eng. Sci. 138 (2015) 244–255, http://dx.doi.org/10.1016/j.ces.2015.07.044.
[22] K. Groß, A. Bieberle, K. Gladyszewski, M. Schubert, U. Hampel, M. Skiborowski, A. Górak, Analysis of flow patterns in high-gravity equipment using Gamma-ray computed tomography, Chem. Ing. Tech. 91 (7) (2019) 1032–1040, http://dx.doi.org/10.1002/cite.201800085.
[23] K. Gładyszewski, K. Groß, A. Bieberle, M. Schubert, M. Hild, A. Górak, M. Skiborowski, Evaluation of performance improvements through application of anisotropic foam packings in rotating packed beds, Chem. Eng. Sci. 230 (2021) 116176, http://dx.doi.org/10.1016/j.ces.2020.116176.
[24] H. Llerena-Chavez, F. Larachi, Analysis of flow in rotating packed beds via CFD simulations—Dry pressure drop and gas flow maldistribution, Chem. Eng. Sci. 64 (9) (2009) 2113–2126, http://dx.doi.org/10.1016/j.ces.2009.01.019.
[25] W. Yang, Y. Wang, J. Chen, W. Fei, Computational fluid dynamic simulation of fluid flow in a rotating packed bed, Chem. Eng. J. 156 (3) (2010) 582–587, http://dx.doi.org/10.1016/j.cej.2009.04.013.
[26] Y. Yang, Y. Xiang, Y. Li, G. Chu, H. Zou, M. Arowo, J. Chen, 3D CFD modelling and optimization of single-phase flow in rotating packed beds, Can. J. Chem. Eng. 93 (6) (2015) 1138–1148, http://dx.doi.org/10.1002/cjce.22183.
[27] J. Wojtasik-Malinowska, M. Jaskulski, M. Jaskulski, CFD simulation of gas pressure drop in porous packing for rotating packed beds (RPB) CO2 absorbers, Environ. Sci. Pollut. Res. 29 (47) (2022) 71857–71870, http://dx.doi.org/10.1007/s11356-022-20859-x.
[28] P. Xie, X. Lu, X. Yang, D. Ingham, L. Ma, M. Pourkashanian, Characteristics of liquid flow in a rotating packed bed for CO2 capture: A CFD analysis, Chem. Eng. Sci. 172 (2017) 216–229, http://dx.doi.org/10.1016/j.ces.2017.06.040.
[29] W. Zhang, P. Xie, Y. Li, L. Teng, J. Zhu, CFD analysis of the hydrodynamic characteristics in a rotating packed bed with multi-nozzles, Chem. Eng. Process. - Process. Intensif. 158 (2020) 108107, http://dx.doi.org/10.1016/j.cep.2020.108107.
[30] R. Rabiee, M. Monzavi, J. Shabanian, A. Shams, S. Golshan, R. Jafari, B. Blais, J. Chaouki, Two-phase flow characterization of a rotating packed bed through CFD simulation in OpenFOAM, Chem. Eng. Sci. 253 (2022) 117589, http://dx.doi.org/10.1016/j.ces.2022.117589.
[31] Y.-C. Yang, Y. Ouyang, N. Zhang, Q.-J. Yu, M. Arowo, A review on computational fluid dynamic simulation for rotating packed beds, J. Chem. Technol. Biotechnol. 94 (4) (2019) 1017–1031, http://dx.doi.org/10.1002/jctb.5880.
[32] W. Zhang, P. Xie, Y. Li, L. Teng, J. Zhu, 3D CFD simulation of the liquid flow in a rotating packed bed with structured wire mesh packing, Chem. Eng. J. 427 (2022) 130874, http://dx.doi.org/10.1016/j.cej.2021.130874.
[33] E. Agostini, G. Boccardo, D. Marchisio, An open-source workflow for open-cell foams modelling: Geometry generation and CFD simulations for momentum and mass transport, Chem. Eng. Sci. 255 (2022) 117583, http://dx.doi.org/10.1016/j.ces.2022.117583.
[34] M. Bracconi, M. Ambrosetti, M. Maestri, G. Groppi, E. Tronconi, A systematic procedure for the virtual reconstruction of open-cell foams, Chem. Eng. J. 315 (2017) 608–620, http://dx.doi.org/10.1016/j.cej.2017.01.069.
[35] F. García Moreno, M. Fromme, J. Banhart, Real-time X-ray radioscopy on metallic foams using a compact micro-focus source, Adv. Eng. Mater. 6 (6) (2004) 416–420, http://dx.doi.org/10.1002/adem.200405143.
[36] L.A. Feldkamp, L.C. Davis, J.W. Kress, Practical cone-beam algorithm, J. Opt. Soc. Amer. A 1 (6) (1984) 612, http://dx.doi.org/10.1364/JOSAA.1.000612.
[37] J. Ahrens, B. Geveci, C. Law, ParaView: An End-User Tool for large data visualization, in: Visualization Handbook, first ed., Elsevier, 2011, pp. 717–731.
[38] C. Lautensack, M. Giertzsch, M. Godehardt, K. Schladitz, Modelling a ceramic foam using locally adaptable morphology, J. Microsc. 230 (3) (2008) 396–404, http://dx.doi.org/10.1111/j.1365-2818.2008.01998.x.
[39] G.D. Wehinger, H. Heitmann, M. Kraume, An artificial structure modeler for 3D CFD simulations of catalytic foams, Chem. Eng. J. 284 (2016) 543–556, http://dx.doi.org/10.1016/j.cej.2015.09.014.
[40] E. Lozano, D. Roehl, W. Celes, M. Gattass, An efficient algorithm to generate random sphere packs in arbitrary domains, Comput. Math. Appl. 71 (8) (2016) 1586–1601, http://dx.doi.org/10.1016/j.camwa.2016.02.032.
[41] C.H. Rycroft, Voro++: A three-dimensional Voronoi cell library in C++, Chaos 19 (4) (2009) 041111, http://dx.doi.org/10.1063/1.3215722.
[42] The CGAL Project, CGAL User and Reference Manual, 5.5.2, CGAL Editorial Board, 2023.
[43] A. Inayat, H. Freund, A. Schwab, T. Zeiser, W. Schwieger, Predicting the specific surface area and pressure drop of reticulated ceramic foams used as catalyst support, Adv. Eng. Mater. 13 (11) (2011) 990–995, http://dx.doi.org/10.1002/adem.201100038.
[44] M.D.M. Innocentini, L.P. Lefebvre, R.V. Meloni, E. Baril, Influence of sample thickness and measurement set-up on the experimental evaluation of permeability of metallic foams, J. Porous Mater. 17 (4) (2010) 491–499, http://dx.doi.org/10.1007/s10934-009-9312-5.
[45] H.G. Weller, G. Tabor, H. Jasak, C. Fureby, A tensorial approach to computational continuum mechanics using object-oriented techniques, Comput. Phys. 12 (6) (1998) 620–631, http://dx.doi.org/10.1063/1.168744.
[46] C. Greenshields, OpenFOAM V10 User Guide, The OpenFOAM Foundation, London, UK, 2022.
[47] F. Menter, T. Esch, Elements of industrial heat transfer predictions, in: 16th Brazilian Congress of Mechanical Engineering, 2001.
[48] F.R. Menter, M. Kuntz, R. Langtry, Ten years of industrial experience with the SST turbulence model, in: K. Hanjalić, Y. Nagano, M.J. Tummers (Eds.), Turbulence, Heat and Mass Transfer 4: Proceedings of the Fourth International Symposium on Turbulence, Heat and Mass Transfer, Antalya, Turkey, 12 - 17 October, 2003, Begell House, New York, NY, 2003.
[49] J. Schöberl, NETGEN an advancing front 2D/3D-mesh generator based on abstract rules, Comput. Vis. Sci. 1 (1) (1997) 41–52, http://dx.doi.org/10.1007/s007910050004.
[50] D.B. Spalding, A single formula for the "Law of the wall", J. Appl. Mech. 28 (3) (1961) 455–458, http://dx.doi.org/10.1115/1.3641728.
[51] S. Calvo, D. Beugre, M. Crine, A. Léonard, P. Marchot, D. Toye, Phase distribution measurements in metallic foam packing using X-ray radiography and micro-tomography, Chem. Eng. Process.: Process. Intensif. 48 (5) (2009) 1030–1039, http://dx.doi.org/10.1016/j.cep.2009.02.001.
[52] P.A. Tipler, G. Mosca, in: J. Wagner (Ed.), Physik, Springer Berlin Heidelberg, Berlin, Heidelberg, 2015, http://dx.doi.org/10.1007/978-3-642-54166-7.
[53] A. Dybbs, R.V. Edwards, A new look at porous media fluid mechanics — Darcy to turbulent, in: J. Bear, M.Y. Corapcioglu (Eds.), Fundamentals of Transport Phenomena in Porous Media, Springer Netherlands, Dordrecht, 1984, pp. 199–256, http://dx.doi.org/10.1007/978-94-009-6175-3_4.